

Optimal Reference Signal Design for Phase Noise Compensation in Multi-carrier Massive MIMO Systems

Vishnu V. Ratnam, *Member, IEEE*.

Abstract

Millimeter-wave and Terahertz frequencies, while promising high throughput and abundant spectrum, are highly susceptible to hardware non-idealities like phase-noise, which degrade the system performance and make transceiver implementation difficult. In this paper, a novel reference-signal (RS) aided low-complexity and low-latency technique is proposed to mitigate phase-noise in high-frequency multi-carrier massive multiple-input-multiple-output systems. Unlike in existing methods, the proposed RS is transmitted in each symbol and occupies adjacent sub-carriers separated from the data by null sub-carriers. The receiver uses the received RS to estimate and compensate for the dominant spectral components of the phase-noise at each symbol. While the null sub-carriers reduce the interference between the RS and data, the frequency compactness of the RS decouples phase-noise estimation from channel equalization, reducing error propagation. A detailed theoretical analysis of the technique is presented and correspondingly, throughput-optimal designs for the RS sequence, RS bandwidth, power allocation and the number of nulled sub-carriers and estimated spectral components, are derived. A hitherto unexplored interplay between oscillator phase-locked loop design and the performance of phase-noise compensation is also studied. Simulations, performed under 3GPP compliant settings, suggest that the proposed scheme, while achieving better performance than several existing solutions, also effectively compensates for oscillator frequency offsets.

Index Terms

Phase noise, phase-locked loop, phase tracking reference signal, millimeter wave, Terahertz, massive MIMO.

V. V. Ratnam is with the Standards and Mobility Innovation Lab at Samsung Research America, Plano, TX, 75023 USA. (e-mail: vishnu.r@samsung.com).

I. INTRODUCTION

Millimeter (mm) and TeraHertz (THz) frequencies offer a huge increase in bandwidth in comparison to conventional sub-6GHz frequencies and are thus strong candidate communication bands to successfully deliver the exponentially rising wireless data traffic [1]. These higher frequencies also enable implementation of massive antenna arrays on small form factors, making massive multiple-input-multiple-output (MIMO) systems practically viable. However, hardware non-idealities like phase-noise (PhN), which is the random fluctuation in the instantaneous frequency of the local oscillators, also tend to increase with the carrier frequency [2], thus degrading the system performance. While low levels of PhN cause a symbol-level channel aging effect, also known as common phase error (CPE) [3], [4], higher levels of PhN additionally induce symbol distortion. This distortion manifests as inter-carrier-interference (ICI) in multi-carrier systems, such as those operating with orthogonal frequency division multiplexing (OFDM) [5]–[7], and can severely limit the signal-to-interference-plus-noise ratio (SINR) gains offered by the massive antenna arrays, at mm-wave/THz frequencies.¹ Consequently, the impact of PhN on multi-carrier massive antenna transceivers has received significant attention in the recent works [3], [9]–[14].

Several PhN compensation techniques for OFDM have been explored in the literature and standardization activities. One class of approaches focus on estimating PhN with minimal pilot overhead, at the expense of a high computational cost and latency. For example, several works estimate PhN and data iteratively using a decision feedback estimation process [6], [7], [15]–[18]. At higher frequencies, where the bandwidth and/or the number of data sub-carriers may be large, this approach may lead to a high computational burden and may also increase system latency. Another class of works have explored non-iterative, pilot-aided estimation approaches [19]–[27], which may be more suitable for mm-wave and THz OFDM systems due to their speed and low computational burden.² For example, [19] explores the mitigation of CPE due to PhN using pilot sub-carriers spread across the system bandwidth, and a similar strategy was adopted by the 3GPP Rel 15 new radio (NR) standard [8]; [20] explores the use of time domain pilots for PhN estimation and [21] additionally identifies the dominant PhN basis for estimation; [22], [23] explore pilot aided joint CPE and channel estimation, with linear interpolation between the pilots; and [24] explores a pilot aided Bayesian estimation of PhN via Kalman smoothing. However such estimation techniques either require prior channel equalization, suffer from inter-symbol-

¹While use of multi-carrier systems at THz is uncertain, 3GPP standards have already adopted OFDM at mm-wave frequencies [8].

²Some of these works also involve an optional decision-directed feedback loop for better performance but with higher complexity.

interference (ISI) and/or may suffer from significant inter-carrier interference (ICI) from the data signals. In contrast to the above schemes, the technique in [25]–[27] involves transmitting a single high power sinusoidal pilot/reference signal (RS), separated from the data sub-carriers by a guard-band, and using the received sub-carriers corresponding to the RS to estimate and compensate for both CPE and ICI in the frequency domain. While the concentration of RS in frequency obviates the need for prior channel estimates, thus preventing estimation error propagation, the guard-band prevents ICI from data sub-carriers and the frequency domain estimation prevents ISI during PhN estimation. Recently, the use of such a sinusoidal RS for joint analog channel estimation and PhN compensation in multi-antenna analog beamforming systems has also been explored [13], [14]. While this PhN estimation technique has also been verified to work experimentally [26], a rigorous theoretical analysis of the same is lacking in prior literature due to the intractable form of PhN spectral coefficients. Such an analysis can, for example, help determine the throughput maximizing values of many system parameters, such as the power allocation to the RS and data, the required guard-band width etc. Furthermore, the use of a strong sinusoidal RS in this technique may also cause a violation of spectral mask regulations.

With the motivation of addressing the aforementioned gaps, in this paper we propose a generalization of the above PhN compensation technique, where the transmitter transmits an arbitrary band-limited RS signal, that occupies adjacent sub-carriers separated from the data sub-carriers by null sub-carriers, and the receiver uses the received RS to estimate the dominant spectral components of PhN in the frequency domain. In addition to decoupling the PhN estimation from channel estimation, such a band-limited RS reduces the null sub-carrier overhead and prevents an increase in the peak-to-average power ratio of the transmit signal, unlike a wide-band RS. By presenting a novel, asymptotically tight approximation to the PhN spectral coefficients, we present a detailed theoretical performance analysis of this PhN compensation technique for an arbitrary RS, and correspondingly find the throughput-optimal power allocation and number of null sub-carriers.³ We also formulate the throughput-optimal RS design problem, and show that signals with good aperiodic auto-correlation properties in the frequency domain, e.g. frequency domain Zero aperiodic Correlation Zone Sequences (ZCZS) [28]–[30] and frequency-domain Barker sequences [31]–[33], are good candidates. Furthermore, we study the impact of oscillator phase-locked loop (PLL) design on PhN estimation, and show that the PLL design objective can be very different for CPE only cancellation and CPE+ISI cancellation. A preliminary observation in this direction was also

³Throughout the paper, we use ‘throughput-optimal’ to refer to solutions that maximize a tight approximation to the system capacity (including the RS overhead).

made recently in [34]. The proposed technique is also consistent with the PhN estimation framework in 3GPP NR Rel 15, where such an RS is referred to as the *phase-tracking reference signal* (PTRS) [8], [35], [36]. However, the current 3GPP PTRS has a different time-frequency pattern and only estimates and compensates for the CPE. The contributions of this paper are as follows:

- 1) We propose a generalized RS aided PhN compensation technique for multi-antenna OFDM systems.
- 2) We characterize the achievable throughput for a multi-antenna hybrid beamforming receiver with the new PhN compensation technique.
- 3) We formulate the throughput-optimal RS design problem and provide optimal solutions.
- 4) We also analytically characterize the throughput-optimal RS bandwidth, power allocation and the numbers of nulled sub-carriers and estimated PhN principal components for the technique.
- 5) We compare of the performance of the scheme to several prior works under practically relevant and 3GPP compliant simulations.
- 6) We also study the interplay between the oscillator PLL bandwidth and the performance of PhN compensation.

The system model is discussed in Section II; the PhN estimation and compensation is discussed in Section III; the signal and noise components of the demodulated outputs are characterized in Section IV; the system throughput is studied in Section V; the optimal RS design is presented in Section VI; other oscillator PhN models are discussed in Section VII; simulation results are provided in Section VIII; and the conclusions are summarized in Section IX.

Notation: scalars are represented by light-case letters; vectors by bold-case letters; and sets by calligraphic letters. Additionally, $j = \sqrt{-1}$, $\mathbb{E}\{\cdot\}$ represents the expectation operator, c^* is the complex conjugate of a complex scalar c , \mathbf{c}^\dagger is the Hermitian transpose of a complex vector \mathbf{c} , $\delta(t)$ represents the Dirac delta function, $\delta_{a,b}^A$ is the modulo- A Kronecker delta function with $\delta_{a,b}^A = 1$ if $a = b \pmod{A}$ and $\delta_{a,b}^A = 0$ otherwise and $\text{Re}\{\cdot\}/\text{Im}\{\cdot\}$ refer to the real/imaginary component, respectively.

II. GENERAL ASSUMPTIONS AND SYSTEM MODEL

We consider the downlink of a single-cell system, with one base-station/transmitter (TX) having M_{tx} antennas and multiple user-equipments/receivers (RXs). While the TX may have arbitrary architecture, each RX is assumed to have a sub-arrayed hybrid beamforming architecture [37], [38], with \bar{M}_{rx} antennas connected to each down-conversion chain via \bar{M}_{rx} phase-shifters, as illustrated in Fig. 1. Furthermore, we assume that the TX allocates one up-conversion chain and one spatially orthogonal datastream to each

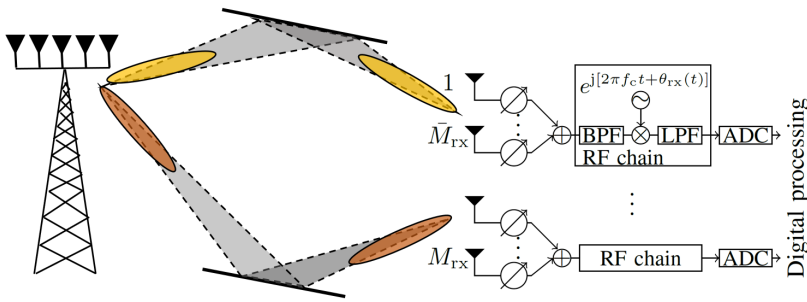


Fig. 1. An illustration of the sub-array based hybrid beamforming architecture at the RX.

RX sub-array. Neglecting the inter-user and inter-datastream interference, we shall restrict the analysis to one representative sub-array of one RX. For this RX sub-array, the TX transmits OFDM symbols with K sub-carriers, indexed as $\mathcal{K} \triangleq \{-K_1, \dots, K_2\}$ where $K = K_1 + K_2 + 1$. Data is transmitted on the $K_1 - g$ lower and $K_2 - g$ higher sub-carriers, i.e. on indices $\mathcal{K} \setminus \mathcal{G}$, where $\mathcal{G} \triangleq \{-g, \dots, 0, \dots, g\}$. The RS for PhN tracking is transmitted on sub-carriers $\hat{\mathcal{G}} \triangleq \{-\hat{g}, \dots, 0, \dots, \hat{g}\}$, where $\hat{g} \leq g$, while the remaining sub-carriers $\mathcal{G} \setminus \hat{\mathcal{G}}$ are nulled to act as a guard-band between the reference and data signals. This transmit structure is illustrated in Fig. 2. Under these conditions, the complex equivalent transmit signal of the 0-th OFDM symbol to the representative RX sub-array can be expressed as:

$$\mathbf{s}_{\text{tx}}(t) = \sqrt{\frac{2}{T_s}} \mathbf{t} \left[\sum_{k \in \hat{\mathcal{G}}} p_k e^{j2\pi f_k t} + \sum_{k \in \mathcal{K} \setminus \mathcal{G}} x_k e^{j2\pi f_k t} \right] e^{j[2\pi f_c t + \theta_{\text{tx}}(t)]}, \quad (1)$$

for $-T_{\text{cp}} \leq t \leq T_s$, where T_s and T_{cp} are the symbol duration and the cyclic prefix duration, respectively, \mathbf{t} is the $M_{\text{tx}} \times 1$ unit-norm TX beamforming vector, p_k is the component of the RS on the k -th subcarrier, x_k is the data signal on the k -th sub-carrier, f_c is the carrier frequency, $f_k = k/T_s$ represents the frequency offset of the k -th sub-carrier and $\theta_{\text{tx}}(t)$ represents the PhN process of the TX oscillator. Here we define the *complex equivalent* signal such that the actual (real) transmit signal is given by $\text{Re}\{\mathbf{s}_{\text{tx}}(t)\}$. For the data sub-carriers ($k \in \mathcal{K} \setminus \mathcal{G}$), we assume the use of independent, zero-mean data streams with equal power allocation $\mathbb{E}\{|x_k|^2\} = E_d$ and for RS we define $E_r \triangleq \sum_{k \in \hat{\mathcal{G}}} |p_k|^2$. The transmit power constraint is then given by $E_r + (K - |\mathcal{G}|)E_d \leq E_s$, where E_s is the total OFDM symbol energy (excluding the cyclic prefix).

The channel to the representative RX sub-array is assumed to have \tilde{L} multi-path components (MPCs), and the corresponding $\bar{M}_{\text{rx}} \times M_{\text{tx}}$ channel impulse response matrix and its Fourier transform, respectively,

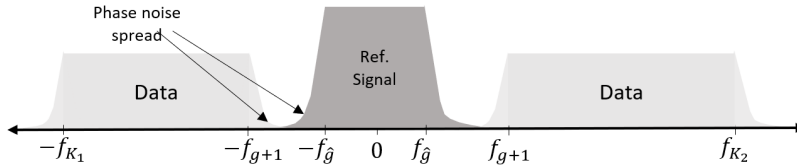


Fig. 2. An illustration of the base-band TX signal with phase noise.

are given as [39]:

$$\mathbf{H}(t) = \sum_{\ell=0}^{\tilde{L}-1} \alpha_{\ell} \mathbf{a}_{\text{rx}}(\ell) \mathbf{a}_{\text{tx}}(\ell)^{\dagger} \delta(t - \tau_{\ell}) \quad (2a)$$

$$\mathcal{H}(f) = \sum_{\ell=0}^{\tilde{L}-1} \alpha_{\ell} \mathbf{a}_{\text{rx}}(\ell) \mathbf{a}_{\text{tx}}(\ell)^{\dagger} e^{-j2\pi(f_c + f)\tau_{\ell}}, \quad (2b)$$

where α_{ℓ} is the complex amplitude, τ_{ℓ} is the delay and $\mathbf{a}_{\text{tx}}(\ell)$, $\mathbf{a}_{\text{rx}}(\ell)$ are the $M_{\text{tx}} \times 1$ TX and $\bar{M}_{\text{rx}} \times 1$ RX sub-array response vectors, respectively, of the ℓ -th MPC. As an illustration, the ℓ -th RX sub-array response vector for a uniform planar sub-array with \bar{M}_{H} horizontal and \bar{M}_{V} vertical elements ($\bar{M}_{\text{rx}} = \bar{M}_{\text{H}}\bar{M}_{\text{V}}$) is given by $\mathbf{a}_{\text{rx}}(\ell) = \tilde{\mathbf{a}}_{\text{rx}}(\psi_{\text{azi}}^{\text{rx}}(\ell), \psi_{\text{ele}}^{\text{rx}}(\ell))$, where:

$$[\tilde{\mathbf{a}}_{\text{rx}}(\psi_{\text{azi}}^{\text{rx}}, \psi_{\text{ele}}^{\text{rx}})]_{\bar{M}_{\text{V}}h+v} = \exp \left\{ j2\pi \frac{\Delta_{\text{H}}h \sin(\psi_{\text{azi}}^{\text{rx}}) \sin(\psi_{\text{ele}}^{\text{rx}})}{\lambda} + j2\pi \frac{\Delta_{\text{V}}(v-1) \cos(\psi_{\text{ele}}^{\text{rx}})}{\lambda} \right\}, \quad (3)$$

for $h \in \{0, \dots, \bar{M}_{\text{H}} - 1\}$ and $v \in \{1, \dots, \bar{M}_{\text{V}}\}$, $\psi_{\text{azi}}^{\text{rx}}(\ell)$, $\psi_{\text{ele}}^{\text{rx}}(\ell)$ are the azimuth and elevation angles of arrival for the ℓ -th MPC, $\Delta_{\text{H}}, \Delta_{\text{V}}$ are the horizontal and vertical antenna spacings and λ is the carrier wavelength. The expression for $\mathbf{a}_{\text{tx}}(\ell)$ can be obtained similarly. We assume the TX and RX to have sufficient prior channel knowledge to implement the analog beamformers \mathbf{t} and \mathbf{r} , respectively. Depending on the analog beamformer design, such knowledge may include either instantaneous [40]–[42] or average channel parameters [43]–[47]. Without loss of generality, let the channel MPCs with non-negligible power along the TX-RX analog beams be indexed as $\{0, \dots, L-1\}$, where $L \leq \tilde{L}$. Due to the large antenna array and associated narrow analog beams at the TX and RX, we assume the effective channel $\mathbf{r}^{\dagger} \mathbf{H}(t) \mathbf{t}$ to have a small delay spread (i.e., $\tau_{L-1} \ll T_s$) and a large coherence bandwidth. Since the TX can afford an accurate oscillator, we also neglect variation of the TX PhN within this small delay spread, i.e., $\theta_{\text{tx}}(t - \tau_{L-1}) \approx \theta_{\text{tx}}(t)$. Additionally we shall also assume that the non-data subcarriers ($k \in \mathcal{G}$) lie within a coherence bandwidth of the effective channel i.e. $T_s/2g \geq \tau_{L-1}$.

The RX sub-array has a low noise amplifier followed by a band-pass filter (BPF) at each antenna, that leaves the desired signal un-distorted but suppresses the out-of-band noise. The filtered signals at each antenna are then phase-shifted by an analog beamformer, combined and down-converted via an RX oscillator and sampled by an analog-to-digital converter (ADC) at K/T_s samples/sec, as depicted in Fig. 1. Assuming perfect timing synchronization at the RX, the sampled received base-band signal for the 0-th OFDM symbol can be expressed as:

$$s_{\text{rx, BB}}[n] = \sum_{\ell=0}^{L-1} \alpha_{\ell} \mathbf{r}^{\dagger} \mathbf{a}_{\text{rx}}(\ell) \mathbf{a}_{\text{tx}}(\ell)^{\dagger} \mathbf{t} \left[\sum_{k \in \hat{\mathcal{G}}} p_k e^{j2\pi f_k (\frac{nT_s}{K} - \tau_{\ell})} + \sum_{k \in \mathcal{K} \setminus \hat{\mathcal{G}}} x_k e^{j2\pi f_k (\frac{nT_s}{K} - \tau_{\ell})} \right] e^{j[\theta_{\text{tx}}[n] + \theta_{\text{rx}}[n]]} + w[n], \quad (4)$$

for $0 \leq n < K$, where the Re/Im parts of $s_{\text{rx, BB}}[n]$ are the outputs corresponding to the in-phase and quadrature-phase components of the RX oscillator, \mathbf{r} is the $\bar{M}_{\text{rx}} \times 1$ unit norm RX beamformer, $\theta_{\text{tx}}[n] \triangleq \theta_{\text{tx}}(nT_s/K)$, $\theta_{\text{rx}}[n]$ is the sampled PhN process of the RX oscillator, $w[n] \sim \mathcal{CN}(0, N_0 K)$ is the post-beamforming *effective* additive Gaussian noise process with independent and identically distributed samples and N_0 is the noise power spectral density. Conventional OFDM demodulation is then performed on the combined base-band signal (4). The demodulated sub-carriers $k \in \hat{\mathcal{G}}$ are used for PhN estimation, while sub-carriers $k \in \mathcal{K} \setminus \hat{\mathcal{G}}$ are used for data demodulation, as discussed in the next section. While prior estimates of the effective channel $\mathbf{r}^{\dagger} \mathbf{H}(t) \mathbf{t}$ are not required for the proposed PhN estimation algorithm in Section III-A, for the purpose of SINR and throughput analysis in Section V we shall assume $\mathbf{r}^{\dagger} \mathbf{H}(t) \mathbf{t}$ can be estimated perfectly at the RX (after PhN compensation).

The PhN of a free-running voltage controlled oscillator (VCO) is quite high and is accurately modeled as a Wiener process [5], [7], [16]. To reduce the resulting PhN, VCOs are therefore usually driven by a PLL, for which several PhN models have been proposed [48], [49]. However, for the convenience of analysis, we shall first model the PhN at the TX and RX as Wiener processes. The extension of the results to PLL based PhN models shall be explored later in Section VII. For the Wiener model, $\theta[n] \triangleq \theta_{\text{tx}}[n] + \theta_{\text{rx}}[n]$ is a non-stationary Gaussian process which satisfies $\theta[n] - \theta[n-1] = w_{\theta}[n]$, where $w_{\theta}[n]$ is zero-mean Gaussian with variance $\sigma_{\theta}^2 T_s / K$, and is independent for each n . We assume the RX to have a priori knowledge of σ_{θ} . Note that in this PhN model, we implicitly assume the mean TX and RX oscillator frequencies to be equal. This assumption shall be relaxed later in Section VIII to demonstrate the oscillator frequency offset suppressing capability of the proposed scheme.

III. PHASE NOISE ESTIMATION AND COMPENSATION

In this section, we first analyze statistics of the channel noise and phase noise, and then discuss the PhN estimation and compensation approach. Note that the sampled channel noise $w[n]$ and the sampled PhN $e^{j\theta[n]}$ for $0 \leq n < K$ can be expressed using their normalized Discrete Fourier Transform (nDFT) coefficients as:

$$w[n] = \sum_{k \in \mathcal{K}} W_k e^{j2\pi kn/K} \quad (5a)$$

$$e^{j\theta[n]} = \sum_{k \in \mathcal{K}} \Omega_k e^{j2\pi kn/K}, \quad (5b)$$

where $W_k = \frac{1}{K} \sum_{n=0}^{K-1} w[n] e^{-j2\pi kn/K}$ and $\Omega_k = \frac{1}{K} \sum_{n=0}^{K-1} e^{-j\theta[n]} e^{-j2\pi kn/K}$ are the corresponding nDFT coefficients. Here nDFT is an unorthodox definition for Discrete Fourier Transform, where the normalization by K is performed while finding W_k, Ω_k instead of in (5). These nDFT coefficients satisfy the following lemmas:

Lemma 1. *The nDFT coefficients of $e^{j\theta[n]}$ are periodic with period K and satisfy:*

$$\sum_{k \in \mathcal{K}} \Omega_{k_1} \Omega_{k_2}^* = \delta_{k_1, k_2}^K, \quad (6a)$$

$$\begin{aligned} \Delta_{k_1, k_2} &\triangleq \mathbb{E}\{\Omega_{k_1} \Omega_{k_2}^*\} \\ &= \frac{1}{K^2} \sum_{\dot{n}, \ddot{n}=0}^{K-1} e^{-\frac{\sigma_\theta^2 |\dot{n} - \ddot{n}| T_s}{2K}} e^{-j2\pi \frac{[k_1 \dot{n} - k_2 \ddot{n}]}{K}} \end{aligned} \quad (6b)$$

$$\approx \frac{\delta_{k_1, k_2}^K}{K} \left[\frac{1 - e^{-\left(\frac{\sigma_\theta^2 T_s - j4\pi k_1}{4}\right)}}{e^{\frac{\sigma_\theta^2 T_s - j4\pi k_1}{2K}} - 1} + \frac{1 - e^{-\left(\frac{\sigma_\theta^2 T_s + j4\pi k_1}{4}\right)}}{1 - e^{-\frac{\sigma_\theta^2 T_s + j4\pi k_1}{2K}}} \right], \quad (6c)$$

for arbitrary integers k_1, k_2 , and the approximation in (6c) is tight for $\sigma_\theta^2 T_s \gg 1$.

Proof. This lemma was first derived by us in [14], and is reproduced in Appendix A for convenience. \square

Lemma 2. *Conditioned upon validity of (6c), $\{\Delta_{k,k} | k \in \mathcal{K}\}$ satisfy:*

$$\Delta_{k,k} \leq \begin{cases} \Delta_{k-2, k-2} & \text{for } 2 \leq k \leq K/2 \\ \Delta_{k+2, k+2} & \text{for } -K \leq k \leq -2 \end{cases}. \quad (7)$$

Proof. See Appendix B \square

Lemma 3. *The nDFT coefficients of $w[n]$, are periodic with period K and are jointly circularly symmetric Gaussian with:*

$$\mathbb{E}\{W_{k_1} W_{k_2}^\dagger\} = \delta_{k_1, k_2}^K N_0, \quad (8)$$

for arbitrary integers k_1, k_2 (see [14] for proof).

The accuracy of the approximation in (6c) is depicted for a typical Wiener PhN process in Fig. 3. As is evident from Fig. 3, (6c) is reasonably accurate for $k_1 = k_2 = \text{odd}$. While there is a mismatch in the value of $\Delta_{k,k}$ for the even sub-carriers with $\sigma_\theta^2 = 1/T_s$, this mismatch vanishes quickly with increasing σ_θ as also shown in Fig. 3 for $\sigma_\theta^2 = 9/T_s$. Even for $k_1 \neq k_2$, we observe that Δ_{k_1, k_2} is around $\sim 20\text{dB}$ lower than Δ_{k_1, k_1} , and thus can reasonably be approximated as 0. Due to the accuracy of these approximations, we shall henceforth assume validity of (6c) in the rest of the analysis.⁴ Then from (4), the received signal

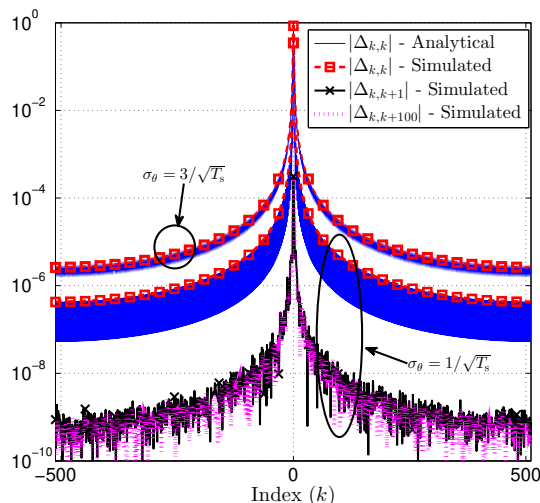


Fig. 3. Comparison of analytical and simulated statistics of the nDFT coefficients of a Wiener PhN process with $T_s = 1\mu\text{s}$, $K_1 = K_2 + 1 = 512$. Simulations averaged over 10^6 realizations.

on sub-carrier k can be expressed as:

$$Y_k = \frac{1}{K} \sum_{n=0}^{K-1} s_{\text{rx, BB}}[n] e^{-j2\pi kn/K} = \sum_{\hat{k} \in \hat{\mathcal{G}}} \beta_0 p_{\hat{k}} \Omega_{k-\hat{k}} + \sum_{\bar{k} \in \mathcal{K} \setminus \hat{\mathcal{G}}} \beta_{\bar{k}} x_{\bar{k}} \Omega_{k-\bar{k}} + W_k, \quad (9)$$

where $\beta_k \triangleq \mathbf{r}^\dagger \mathcal{H}(f_k) \mathbf{t}$ and we use $\beta_{\hat{k}} \approx \beta_0$ for $\hat{k} \in \hat{\mathcal{G}}$, which is reasonable due to the large coherence bandwidth of the effective channel (see Section II). As is evident from (9), the sub-carrier output Y_k

⁴The results presented in the paper do not depend on the exact expression for $\Delta_{k,k}$. Thus, if the accuracy of $\Delta_{k,k}$ in (6c) is insufficient for a specific scenario, it can be replaced by the exact value from (6b).

contains contributions from other data-subcarriers, i.e., it suffers from ICI and phase rotation/CPE due to the PhN, which can be suppressed by PhN estimation as discussed next.

A. Phase noise estimation

From Lemma 2 and Fig. 3, we observe that the magnitude of $\Delta_{k,k}$ decreases quickly with $|k|$, and therefore the PhN nDFT coefficients for lower frequency indices dominate its behavior and impact. In fact, from (6c), these indices form the principal components of the PhN process. Consequently, we shall only estimate Ω_k for the dominant principal components: $k \in \mathcal{U}$, where $\mathcal{U} = \{-u, \dots, u\}$. Here u is a design parameter whose throughput-optimal value shall be discussed later in Section VI. These coefficients $\{\Omega_k | k \in \mathcal{U}\}$ are estimated from the sub-carrier outputs $\{Y_k | |k| \leq \hat{g} + u\}$. To reduce ICI from the data sub-carriers to these sub-carrier outputs, we assume that the number of null sub-carriers \mathcal{G} is designed such that $g \geq \hat{g} + 2u$. Then from (9), the received signal on sub-carrier $k \in [-\hat{g} - u, \hat{g} + u]$ can be expressed as:

$$\begin{aligned} Y_k &\stackrel{(1)}{\approx} \beta_0 \left[\sum_{\hat{g}=-\hat{g}}^{\hat{g}} p_{\hat{g}} \Omega_{k-\hat{g}} \right] + W_k \\ &\stackrel{(2)}{\approx} \beta_0 \left[\sum_{\hat{g}=\max\{-\hat{g}+k, -\hat{g}\}}^{\min\{\hat{g}+k, \hat{g}\}} p_{k-\hat{g}} \Omega_{\hat{g}} \right] + W_k, \end{aligned} \quad (10)$$

where $\stackrel{(1)}{\approx}$ follows by neglecting ICI due to data sub-carriers and $\stackrel{(2)}{\approx}$ follows by approximating $\Omega_k \approx 0$ for $|k| > u$. Note that these approximations are tight for sufficiently large u, g . We shall henceforth assume validity of the approximation in (10) for the rest of the analysis. Equation (10) can then be expressed in matrix form as:

$$\mathbf{Y}^{(u)} = \beta_0 \mathbf{P}^{(u)} \boldsymbol{\Omega}^{(u)} + \mathbf{W}^{(u)}, \quad (11)$$

where $\mathbf{Y}^{(u)}, \mathbf{W}^{(u)}$ are $(2\hat{g} + 2u + 1) \times 1$ matrices with the i -th entries being $Y_{i-\hat{g}-u-1}$ and $W_{i-\hat{g}-u-1}$, respectively, $\boldsymbol{\Omega}^{(u)}$ is a $(2u + 1) \times 1$ matrix with $[\boldsymbol{\Omega}^{(u)}]_i = \Omega_{i-u-1}$ and $\mathbf{P}^{(u)}$ is a $(2\hat{g} + 2u + 1) \times (2u + 1)$ rectangular, banded Toeplitz matrix with $[\mathbf{P}^{(u)}]_{ij} = p_{-\hat{g}+i-j}$ for $0 \leq i-j \leq 2\hat{g}$ and $[\mathbf{P}^{(u)}]_{ij} = 0$ otherwise.

Assuming $\mathbf{R}_p \triangleq [\mathbf{P}^{(u)}]^\dagger \mathbf{P}^{(u)}$ to be full rank, the least squares (LS) estimate for $\beta_0 \boldsymbol{\Omega}^{(u)}$ can be obtained as:

$$\widehat{\beta_0 \boldsymbol{\Omega}^{(u)}} = \mathbf{R}_p^{-1} [\mathbf{P}^{(u)}]^\dagger \mathbf{Y}^{(u)} = \beta_0 \boldsymbol{\Omega}^{(u)} + \widehat{\mathbf{W}}^{(u)}, \quad (12)$$

where $\hat{\mathbf{W}}^{(u)} \sim \mathcal{CN}\left(\mathbb{O}_{(2u+1 \times 1)}, \mathbf{R}_p^{-1} \mathbf{N}_0\right)$. Note that the LS estimate in (12) does not require knowledge of β_0 and is thus decoupled from channel estimation. This prevents channel estimation errors (with ICI) from crawling into the PhN estimates i.e. error propagation. While linear minimum mean square error (LMMSE) estimation of $\Omega^{(u)}$ may lead to less sum square error accumulation than with LS estimation, we do not consider it here for analytical tractability. A comparison of the two estimators is performed via simulations later in Section VIII. As shall be shown, optimizing the choice of u enables limiting noise accumulation of the LS estimator, this achieving almost identical performance to the LMMSE estimator.

B. Phase noise compensation

To compensate for the phase rotation and ICI, a simple PhN compensation technique is considered, where the k -th OFDM output (after compensation) can be obtained as:

$$\begin{aligned} \hat{Y}_k &= \sum_{\hat{u} \in \mathcal{U}} \left[\widehat{\beta_0 \Omega^{(u)}} \right]_{\hat{u}+u+1}^* Y_{k+\hat{u}} \\ &= \sum_{\hat{u} \in \mathcal{U}} [\beta_0^* \Omega_{\hat{u}}^* + \hat{W}_{\hat{u}}^*] \left[\sum_{\hat{k} \in \hat{\mathcal{G}}} \beta_0 p_{\hat{k}} \Omega_{k+\hat{u}-\hat{k}} + \sum_{\bar{k} \in \mathcal{K} \setminus \mathcal{G}} \beta_{\bar{k}} x_{\bar{k}} \Omega_{k+\hat{u}-\bar{k}} + W_{k+\hat{u}} \right], \end{aligned} \quad (13)$$

where we use (12) and define $\hat{W}_{\hat{u}} \triangleq [\hat{\mathbf{W}}^{(u)}]_{\hat{u}-u-1}$. These PhN compensated sub-carriers $\{\hat{Y}_k | k \in \mathcal{K} \setminus \mathcal{G}\}$ are then used to demodulate the data signals x_k . Using (6a), it can be readily shown that the above technique can completely cancel the PhN in the absence of estimation noise $\hat{\mathbf{W}}^{(u)}$ in (12) and for $u \gg 1$. The demodulated outputs in the more general case are analyzed in the next section. Note that CPE-only compensation [19], [50] is a special case of (13), obtained by picking $u = 0$.

IV. ANALYSIS OF THE DEMODULATED OUTPUTS

We shall split \hat{Y}_k in (13) as $\hat{Y}_k = \hat{S}_k + \hat{I}_k + \hat{Z}_k$ where \hat{S}_k , referred to as the signal component, involves the terms in (13) containing x_k and not containing the channel/estimation noise, \hat{I}_k , referred to as the interference component, involves the terms containing $\{p_{\hat{k}}, x_{\bar{k}} | \hat{k} \in \hat{\mathcal{G}}, \bar{k} \in \mathcal{K} \setminus \{k\}\}$ and not containing the channel/estimation noise, and \hat{Z}_k , referred to as the noise component, containing the remaining terms. These signal, interference and noise components are analyzed in the following subsections. Note that while the mathematical tools from our prior work [14] can be directly extended to analyze \hat{Y}_k for the case of $\hat{g} = 0$ (i.e. sinusoidal RS), the generic case handled here requires novel analysis techniques.

A. Signal component analysis

From (13), the signal component for $k \in \mathcal{K} \setminus \mathcal{G}$ can be expressed as:

$$\hat{S}_k = \sum_{\dot{u} \in \mathcal{U}} \beta_0^* \beta_k x_k |\Omega_{\dot{u}}|^2. \quad (14)$$

As is evident, the phase rotation due the PhN is suppressed by the compensation technique and the magnitude of signal component increases with u . Taking an expectation with respect to the PhN and x_k , the energy of the signal component can be obtained as:

$$\mathbb{E}\{|\hat{S}_k|^2\} = |\beta_0 \beta_k|^2 E_d \mathbb{E}\left\{\left|\sum_{\dot{u} \in \mathcal{U}} |\Omega_{\dot{u}}|^2\right|^2\right\} \geq |\beta_0 \beta_k|^2 E_d \mu(0, u)^2, \quad (15)$$

where $\mu(a, b) \triangleq \sum_{\dot{u}=-b}^b \Delta_{a+\dot{u}, a+\dot{u}}$, and the last step follows from Jensen's inequality and (6c).

B. Interference component analysis

From (13), the interference component for $k \in \mathcal{K} \setminus \mathcal{G}$ can be expressed as:

$$\hat{I}_k = \sum_{\dot{u} \in \mathcal{U}} \sum_{\dot{k} \in \hat{\mathcal{G}}} |\beta_0|^2 p_{\dot{k}} \Omega_{\dot{u}}^* \Omega_{k+\dot{u}-\dot{k}} + \sum_{\dot{u} \in \mathcal{U}} \sum_{\bar{k} \in \mathcal{K} \setminus [\mathcal{G} \cup \{k\}]} \beta_0^* \beta_{\bar{k}} x_{\bar{k}} \Omega_{\dot{u}}^* \Omega_{k+\dot{u}-\bar{k}}. \quad (16)$$

The first and second moment of \hat{I}_k , averaged over the PhN and $\{x_{\bar{k}} | \bar{k} \neq k\}$ can be expressed as:

$$\begin{aligned} \mathbb{E}\{\hat{I}_k\} &\stackrel{(1)}{=} 0 \\ \mathbb{E}\{|\hat{I}_k|^2\} &\stackrel{(2)}{=} \mathbb{E}\left[\sum_{\dot{u} \in \mathcal{U}} \Omega_{\dot{u}}^* \left[\sum_{\dot{k} \in \hat{\mathcal{G}}} p_{\dot{k}} |\beta_0|^2 \Omega_{k+\dot{u}-\dot{k}}\right]\right]^2 + \sum_{\bar{k} \in \mathcal{K} \setminus [\mathcal{G} \cup \{k\}]} |\beta_0^* \beta_{\bar{k}}|^2 E_d \mathbb{E}\left[\sum_{\dot{u} \in \mathcal{U}} \Omega_{\dot{u}}^* \Omega_{k+\dot{u}-\bar{k}}\right]^2 \\ &\stackrel{(3)}{\leq} \mathbb{E}\left\{\left[\sum_{\dot{u} \in \mathcal{U}} |\Omega_{\dot{u}}|^2\right] \left[\sum_{\dot{u} \in \mathcal{U}} \left|\sum_{\dot{k} \in \hat{\mathcal{G}}} p_{\dot{k}} |\beta_0|^2 \Omega_{k+\dot{u}-\dot{k}}\right|^2\right]\right\} \\ &\quad + \sum_{\dot{u}, \ddot{u} \in \mathcal{U}} |\beta_0 \bar{\beta}|^2 E_d \mathbb{E}\left\{\Omega_{\dot{u}}^* \left[\sum_{\bar{k} \in \mathcal{K} \setminus \{k\}} \Omega_{k+\dot{u}-\bar{k}} \Omega_{k+\ddot{u}-\bar{k}}^*\right] \Omega_{\ddot{u}}\right\} \\ &\stackrel{(4)}{\leq} \mathbb{E}\left[\sum_{\dot{u} \in \mathcal{U}} \left|\sum_{\dot{k} \in \hat{\mathcal{G}}} p_{\dot{k}} |\beta_0|^2 \Omega_{k+\dot{u}-\dot{k}}\right|^2\right] + \sum_{\dot{u}, \ddot{u} \in \mathcal{U}} |\beta_0 \bar{\beta}|^2 E_d \mathbb{E}\left[\delta_{\dot{u}, \ddot{u}}^K \Omega_{\dot{u}}^* \Omega_{\ddot{u}} - |\Omega_{\dot{u}}|^2 |\Omega_{\ddot{u}}|^2\right] \\ &\stackrel{(5)}{\leq} \sum_{\dot{k} \in \hat{\mathcal{G}}} |p_{\dot{k}}|^2 |\beta_0|^4 \mu(k - \dot{k}, u) + |\beta_0 \bar{\beta}|^2 E_d [\mu(0, u) - \mu(0, u)^2], \quad (17) \end{aligned}$$

where $\stackrel{(1)}{=}$ follows from $k > g \geq \hat{g} + 2u$, (6a) and the zero mean assumption for data; $\stackrel{(2)}{=}$ also follows from the independent, zero mean assumption for sub-carrier data; $\stackrel{(3)}{\leq}$ follows by using the Cauchy-Schwartz inequality for the first term and defining $\bar{\beta} \triangleq \max_{k \in \mathcal{K}} |\beta_k|$; $\stackrel{(4)}{\leq}$ follows by using (6a) for both the terms; and $\stackrel{(5)}{=}$ follows by using Jensen's inequality for the second term and (6c) for both terms. Despite being in closed form, equation (17) usually yields a loose bound on $\mathbb{E}\{|I_k|^2\}$ for $|k| \ll K$, as also observed in [14] for the case of $\hat{g} = 0$.

Remark IV.1. A tighter approximation is obtained by replacing $\mu(k - \hat{k}, u)$ in (17) by $\tilde{\mu}(k - \hat{k}, u)$ where $\tilde{\mu}(a, u) \triangleq \sum_{\dot{u} \in \mathcal{U}} \Delta_{\dot{u}, \dot{u}} \Delta_{\dot{u}+a, \dot{u}+a}$.

This heuristic is obtained by assuming $\Omega_{\dot{u}}$ and $\Omega_{k+\dot{u}-\hat{k}}$ to be independently distributed in step $\stackrel{(2)}{=}$ of (17), but we skip the proof for brevity. As shall be verified in Section VIII, Remark IV.1 offers a tighter approximation to $\mathbb{E}\{|\hat{I}_k|^2\}$ and hence we shall use $\tilde{\mu}(k, \hat{g})$ instead of $\mu(k, \hat{g})$ in the forthcoming derivations in Section V.

C. Noise component analysis

The noise component of the received signal on subcarrier $k \in \mathcal{K} \setminus \mathcal{G}$ can be expressed as:

$$\hat{Z}_k = \hat{Z}_k^{(1)} + \hat{Z}_k^{(2)} + \hat{Z}_k^{(3)} + \hat{Z}_k^{(4)}, \text{ where:}$$

$$\hat{Z}_k^{(1)} = \sum_{\dot{u} \in \mathcal{U}} \sum_{\hat{k} \in \hat{\mathcal{G}}} \hat{W}_{\dot{u}}^* \beta_0 p_{\hat{k}} \Omega_{k+\dot{u}-\hat{k}} \stackrel{(1)}{=} \sum_{v=-\hat{g}-u}^{\hat{g}+u} \sum_{\dot{u}=-\min\{u, v+\hat{g}\}}^{\min\{u, \hat{g}-v\}} \hat{W}_{\dot{u}}^* \beta_0 p_{v+\dot{u}} \Omega_{k-v} \quad (18a)$$

$$\hat{Z}_k^{(2)} = \sum_{\dot{u} \in \mathcal{U}} \sum_{\bar{k} \in \mathcal{K} \setminus \mathcal{G}} \hat{W}_{\dot{u}}^* \beta_{\bar{k}} x_{\bar{k}} \Omega_{k+\dot{u}-\bar{k}} \quad (18b)$$

$$\hat{Z}_k^{(3)} = \sum_{\dot{u} \in \mathcal{U}} \beta_0^* \Omega_{\dot{u}}^* W_{k+\dot{u}} \quad (18c)$$

$$\hat{Z}_k^{(4)} = \sum_{\dot{u} \in \mathcal{U}} \hat{W}_{\dot{u}}^* W_{k+\dot{u}}, \quad (18d)$$

where $\stackrel{(1)}{=}$ is obtained by using change of variables $v = \hat{k} - \dot{u}$. From Lemma 3 and equations (10)–(12), it can be readily verified that $\hat{W}_{\dot{u}}$ and W_k are circularly symmetric, zero-mean Gaussian and mutually independent for $\dot{u} \in \mathcal{U}, k \in \mathcal{K} \setminus \mathcal{G}$. Therefore the first and second moments of the noise signal, averaged over the PhN, channel noise and data signals, can be expressed as:

$$\mathbb{E}\{\hat{Z}_k\} = 0 \quad (19a)$$

$$\mathbb{E}\{|\hat{Z}_k|^2\} = \sum_{i=1}^4 \mathbb{E}\{|\hat{Z}_k^{(i)}|^2\}, \quad (19b)$$

where:

$$\begin{aligned} \mathbb{E}\{|\hat{Z}_k^{(1)}|^2\} &\stackrel{(1)}{=} \sum_{v=-\hat{g}-u}^{\hat{g}+u} \Delta_{k-v, k-v} \mathbb{E} \left| \sum_{\dot{u}=-\min\{u, v+\hat{g}\}}^{\min\{u, \hat{g}-v\}} \hat{W}_{\dot{u}}^* \beta_0 p_{v+\dot{u}} \right|^2 \\ &\stackrel{(2)}{\leq} \sum_{v=-\hat{g}-u}^{\hat{g}+u} \eta_{k, \hat{g}+u} \sum_{\dot{u}, \ddot{u}=-\min\{u, v+\hat{g}\}}^{\min\{u, \hat{g}-v\}} |\beta_0|^2 N_0 R_p^{\text{inv}}(\ddot{u}, \dot{u}) p_{v+\dot{u}} p_{v+\ddot{u}}^* \\ &\stackrel{(3)}{=} \eta_{k, \hat{g}+u} \sum_{\dot{u}, \ddot{u} \in \mathcal{U}} |\beta_0|^2 N_0 R_p^{\text{inv}}(\ddot{u}, \dot{u}) \sum_{v=-\hat{g}-\min\{\dot{u}, \ddot{u}\}}^{\hat{g}-\min\{\dot{u}, \ddot{u}\}} p_{v+\dot{u}} p_{v+\ddot{u}}^* \\ &\stackrel{(4)}{=} \eta_{k, \hat{g}+u} \sum_{\dot{u}, \ddot{u} \in \mathcal{U}} |\beta_0|^2 N_0 R_p^{\text{inv}}(\ddot{u}, \dot{u}) R_p(\dot{u}, \ddot{u}) = \eta_{k, \hat{g}+u} |\mathcal{U}| |\beta_0|^2 N_0 \end{aligned} \quad (20a)$$

$$\begin{aligned} \mathbb{E}\{|\hat{Z}_k^{(2)}|^2\} &= \sum_{\dot{u} \in \mathcal{U}} R_p^{\text{inv}}(\dot{u}, \dot{u}) \left[\sum_{\bar{k} \in \mathcal{K} \setminus \mathcal{G}} |\beta_{\bar{k}}|^2 E_d \Delta_{k+\dot{u}-\bar{k}, k+\dot{u}-\bar{k}} \right] N_0 \\ &\leq \sum_{\dot{u} \in \mathcal{U}} R_p^{\text{inv}}(\dot{u}, \dot{u}) \left[\sum_{\bar{k} \in \mathcal{K}} |\bar{\beta}|^2 E_d \Delta_{k+\dot{u}-\bar{k}, k+\dot{u}-\bar{k}} \right] N_0 \\ &\stackrel{(5)}{=} \text{Tr}\{\mathbf{R}_p^{-1}\} N_0 |\bar{\beta}|^2 E_d \end{aligned} \quad (20b)$$

$$\mathbb{E}\{|\hat{Z}_k^{(3)}|^2\} \stackrel{(6)}{=} \sum_{\dot{u} \in \mathcal{U}} |\beta_0|^2 \Delta_{\dot{u}, \dot{u}} N_0 = |\beta_0|^2 \mu(0, u) N_0 \quad (20c)$$

$$\mathbb{E}\{|\hat{Z}_k^{(4)}|^2\} \stackrel{(7)}{=} \sum_{\dot{u} \in \mathcal{U}} R_p^{\text{inv}}(\dot{u}, \dot{u}) N_0^2 = \text{Tr}\{\mathbf{R}_p^{-1}\} N_0^2, \quad (20d)$$

where $\stackrel{(1)}{=}$ follows from (6a); $\stackrel{(2)}{\leq}$ follows by defining $\eta_{a,b} \triangleq \max_{-b \leq c \leq b} \{\Delta_{a+c, a+c}\}$, the function $R_p^{\text{inv}}(a, b) \triangleq [\mathbf{R}_p^{-1}]_{2u+1+a, 2u+1+b}$ and using the definition of $\hat{\mathbf{W}}^{(u)}$ in (12); $\stackrel{(3)}{=}$ follows by changing the order of summation of v, \dot{u}, \ddot{u} ; $\stackrel{(4)}{=}$ follows from the definition of \mathbf{R}_p and by defining $R_p(a, b) \triangleq [\mathbf{R}_p]_{2u+1+a, 2u+1+b}$; $\stackrel{(5)}{=}$ follows from (6a); $\stackrel{(6)}{=}$ follows from definition of $\mu(\cdot)$ in (15) and $\stackrel{(7)}{=}$ follows by observing that $\hat{W}_{\dot{u}}$ and $W_{k+\dot{u}}$ are independent for $k \in \mathcal{K} \setminus \mathcal{G}$ (from (8)).

V. PERFORMANCE ANALYSIS

From the analysis in the previous section, the effective channel between the k -th OFDM input and the k -th demodulated output (after PhN compensation) can be expressed as:

$$\hat{Y}_k = \sum_{\hat{u} \in \mathcal{U}} \beta_0^* \beta_k x_k |\Omega_{\hat{u}}|^2 + \hat{I}_k + \hat{Z}_k, \quad (21)$$

where the statistics of the \hat{I}_k, \hat{Z}_k are discussed in Section IV. Note that the signal component in (21) experiences a channel dependent fading $\beta_0^* \beta_k$ and a PhN dependent fading coefficient $\sum_{\hat{u} \in \mathcal{U}} |\Omega_{\hat{u}}|^2$. The estimation of these coefficients shall be discussed later in this section. While the noise term $\hat{Z}_k^{(2)}$ also depends on x_k (see (18b)), its contribution is negligible for $K \gg 1$. Thus, we can reasonably assume $\hat{I}_k + \hat{Z}_k$ to be conditionally independent of the signal component, given $\sum_{\hat{u} \in \mathcal{U}} \Omega_{\hat{u}}$. Assuming perfect estimates of the fading coefficients at the RX and using (15), a lower bound to the SINR for sub-carrier $k \in \mathcal{K} \setminus \mathcal{G}$ can then be expressed as:

$$\Gamma_k^{\text{LB}} = \frac{|\beta_0 \beta_k|^2 E_d \mu(0, u)^2}{\bar{\sigma}_{I_k}^2 + \bar{\sigma}_{Z_k}^2}, \quad (22)$$

where $\bar{\sigma}_{I_k}^2, \bar{\sigma}_{Z_k}^2$ are obtained from the upper bounds in (17) and (20). In a similar way, the system ergodic capacity can be expressed as:⁵

$$\begin{aligned} C(\boldsymbol{\beta}) &\stackrel{(1)}{=} \frac{1}{K} \sum_{k \in \mathcal{K} \setminus \mathcal{G}} \mathbb{E}_{\boldsymbol{\Omega}} \left[\mathcal{H}(\hat{Y}_k | \boldsymbol{\Omega}) - \mathcal{H}(\hat{I}_k + \hat{Z}_k | \boldsymbol{\Omega}) \right] \\ &\stackrel{(2)}{\geq} \frac{1}{K} \sum_{k \in \mathcal{K} \setminus \mathcal{G}} \mathbb{E}_{\boldsymbol{\Omega}} \left[\log \left(\mathbb{E} \left\{ |\hat{S}_k|^2 + |\hat{I}_k + \hat{Z}_k|^2 \mid \boldsymbol{\Omega} \right\} \right) - \log \left(\mathbb{E} \left\{ |\hat{I}_k + \hat{Z}_k|^2 \mid \boldsymbol{\Omega} \right\} \right) \right] \\ &\stackrel{(3)}{\approx} \frac{1}{K} \sum_{k \in \mathcal{K} \setminus \mathcal{G}} \log(1 + \Gamma_k^{\text{LB}}) \triangleq C^{\text{LB1}}(\boldsymbol{\beta}), \end{aligned} \quad (23)$$

where $\stackrel{(1)}{\geq}$ follows by defining $\mathcal{H}(\cdot)$ as the differential entropy, $\boldsymbol{\Omega}$ as the vector of all nDFT coefficients in (5b) and using the expression for ergodic capacity [52]; $\stackrel{(2)}{\geq}$ is obtained by noting that, conditioned on $\boldsymbol{\Omega}$, \hat{S}_k is zero-mean Gaussian and independent of $\hat{I}_k + \hat{Z}_k$ and that a Gaussian $\hat{I}_k + \hat{Z}_k$ minimizes capacity [53]; and $\stackrel{(3)}{\approx}$ follows by sending the outer expectation into the $\log(\cdot)$ functions. While $\stackrel{(3)}{\approx}$ is an approximation in general, it can be shown using Jensen's inequality that it yields a lower bound for

⁵Here the ergodic capacity is computed assuming $\{\beta_k | k \in \mathcal{K}\}$ remain constant for infinite time but the PhN $\boldsymbol{\Omega}$ experiences many independent realizations. This capacity is representative of the throughput of practical codes that have a length spanning multiple OFDM symbols but smaller than coherence time of β_k [51].

sufficiently large u . This is because $|\hat{S}_k|^2$ experiences minimal variation with Ω , as evidenced by the facts that $\text{Variance}\{\sum_{\hat{u} \in \mathcal{U}} |\Omega[\hat{u}]|^2\} \leq \mu(0, u)[1 - \mu(0, u)]$ (from (6a) and [54]), and $\mu(0, u) \approx 1$ (from Lemmas 1-2 and Fig. 3).

Note that for demodulating x_k 's from (21) and achieving the above SINR and capacity, the RX requires estimates of channel dependent coefficients $\{\beta_0^* \beta_k | k \in \mathcal{K}\}$, N_0 and the PhN dependent fading coefficient $\sum_{\hat{u} \in \mathcal{U}} |\Omega_{\hat{u}}|^2$. Since the ICI is suppressed in (22), the channel parameters β, N_0 can be tracked accurately at the RX using pilot sub-carriers and blanked sub-carriers, respectively. These values, along with PhN parameter σ_θ , can further be fed back to the TX for rate and power allocation. On the other hand, the PhN dependent, low variance, fast varying component $\sum_{\hat{u} \in \mathcal{U}} |\Omega[\hat{u}]|^2$ can to be estimated from (12) as:

$$\left[[\hat{\Omega}^{(u)}]^\dagger \hat{\Omega}^{(u)} - \text{Tr}\{\mathbf{R}_p^{-1} N_0\} \right] / |\beta_0|^2 \quad (24)$$

where the second term removes the bias due to the noise: $\mathbb{E}\{\mathbf{W}^{(u)\dagger} \mathbf{W}^u\}$.

VI. OPTIMAL RS DESIGN AND SYSTEM PARAMETERS

In this section, we find the conditionally throughput-optimal designs of each of the 4 RS parameters: $\hat{g}, \{p_{-\hat{g}}, \dots, p_{\hat{g}}\}, E_r$ and u , while the remaining 3 parameters are held constant. The joint optimal values of all 4 parameters can then be obtained simply by iterating through these designs.⁶

Note that (23) is a strictly decreasing function of g for fixed \hat{g}, u . Thus we shall henceforth assume $g = \hat{g} + 2u$ viz., its lowest allowed value from Section III-A. For given E_r and $\text{Tr}\{\mathbf{R}_p^{-1}\}$, we also observe from (17)–(23) that $C^{\text{LB1}}(\beta)$ is a decreasing function of \hat{g} . Thus, $\hat{g} = 0$ (a purely sinusoidal RS) maximizes $C^{\text{LB1}}(\beta)$, wherein all of E_r is allocated to a single sub-carrier. However, spectral mask regulations may often set an upper limit \bar{E} on the power allocated to a single sub-carrier. Thus for a given RS power E_r per symbol, the throughput-optimal choice of \hat{g} is $\hat{g}^{\text{opt}} = \left\lceil \frac{E_r}{2\bar{E}} - 1 \right\rceil$.

While $C^{\text{LB1}}(\beta)$ in (23) is in closed form, its dependence on sub-carrier index k makes it difficult to find near optimal $\{p_{-\hat{g}}, \dots, p_{\hat{g}}\}, E_r$ and u . Fortunately, as detailed in Appendix C, a further lower bound $C^{\text{LB2}}(\beta) \leq C^{\text{LB1}}(\beta)$ can be obtained as:

$$C^{\text{LB2}}(\beta) \triangleq \sum_{k \in \mathcal{K} \setminus \mathcal{G}} \left[\frac{\log(|\beta_0 \beta_k|^2)}{K} + \frac{\log[\mu(0, u)^2 \Xi(\beta)]}{K} \right], \text{ where:} \quad (25)$$

⁶In a practical scenario, several of these parameters may be pre-determined constants, thereby obviating the need to iterate through them.

$$\frac{1}{\Xi(\boldsymbol{\beta})} \triangleq \left[\frac{E_s |\beta_0 \bar{\beta}|^2}{K - |\mathcal{G}|} \mu(0, u) [1 - \mu(0, u)] + |\beta_0|^2 N_0 + \text{Tr}\{\mathbf{R}_p^{-1}\} N_0 (|\bar{\beta}|^2 E_d + N_0) \right] / E_d. \quad (26)$$

For this bound, we have the following theorem.

Theorem 1. For given E_r, u and \hat{g} , $C^{\text{LB}2}(\boldsymbol{\beta})$ is maximized by a RS such that the sequence $\{p_{-\hat{g}}, p_{-\hat{g}+1}, \dots, p_{\hat{g}}\}$ has zero aperiodic autocorrelation for shifts $\in \{-2u, \dots, 2u\} \setminus \{0\}$.

Proof. Note that for given E_r, u and \hat{g} , $C^{\text{LB}2}(\boldsymbol{\beta})$ is maximized by a RS with minimum $\text{Tr}\{\mathbf{R}_p^{-1}\}$. Now from the definition of \mathbf{R}_p in (12), it follows that:

$$\begin{aligned} \text{Tr}\{\mathbf{R}_p\} &= \sum_{\dot{u} \in \mathcal{U}} \lambda_{\dot{u}}^p = |\mathcal{U}| E_r \\ \Rightarrow \text{Tr}\{\mathbf{R}_p^{-1}\} &= |\mathcal{U}| \sum_{\dot{u} \in \mathcal{U}} \frac{1}{|\mathcal{U}|} [\lambda_{\dot{u}}^p]^{-1} \geq \frac{|\mathcal{U}|}{E_r}, \end{aligned} \quad (27)$$

where $\lambda_{\dot{u}}^p$ is the \dot{u} -th eigenvalue of \mathbf{R}_p , and (27) follows from convexity of $f(x) = 1/x$ for $x > 0$ and Jensen's inequality. Eqn (27) is satisfied with equality iff $\lambda_{\dot{u}}^p = E_r \forall \dot{u} \in \mathcal{U}$. Since \mathbf{R}_p is also Hermitian symmetric, this implies (27) is met with equality iff $\mathbf{R}_p = E_r \mathbb{I}_{2u+1}$. Finally, observing that

$$[\mathbf{R}_p]_{a,b} = \sum_{i=-\hat{g}+\max\{a,b\}}^{\hat{g}+\min\{a,b\}} p_{i-a}^* p_{i-b}, \quad \text{for } 1 \leq a, b \leq 2u+1,$$

the theorem follows. \square

Sequences \mathbf{p} that satisfy criterion in Theorem 1 are referred to as Zero aperiodic Correlation Zone Sequences (ZCZS) [28]–[30], where the ‘zero correlation zone’ involves the shifts $\{-2u, \dots, 2u\} \setminus \{0\}$. Note that for $\hat{g} = 0$, this criterion is always satisfied. While such a ZCZS sequence may not exist for all values of \hat{g} and u , a close approximation is provided by generalized Barker sequences [31]–[33], which ensure that the magnitude of the aperiodic autocorrelation of \mathbf{p} is $\leq E_r/|\hat{\mathcal{G}}|$ for all non-zero shifts. For the case of $\hat{g} \gg u$, sequences with zero *periodic* autocorrelation such as Zadoff-Chu sequences or m-sequences [55] may also serve as good candidates. Assuming the use of such good sequences for the RS, we shall henceforth approximate $\text{Tr}\{\mathbf{R}_p^{-1}\} \approx |\mathcal{U}|/E_r$.

Using $\text{Tr}\{\mathbf{R}_p^{-1}\} = |\mathcal{U}|/E_r$ and $E_d = (E_s - E_r)/(K - |\mathcal{G}|)$ in (26), it can be readily verified that the numerator of $\Xi(\boldsymbol{\beta})$ is a positive, affine decreasing function of E_r and the denominator is a positive, differentiable, strictly convex function of E_r . Thus $\Xi(\boldsymbol{\beta})$ is strictly pseudoconcave in E_r [56], and for given \hat{g} and u , the $C^{\text{LB}2}(\boldsymbol{\beta})$ -maximizing power allocation can be obtained by setting $\partial \Xi(\boldsymbol{\beta}) / \partial E_r = 0$

as:

$$E_r^{\text{opt}} = E_s \frac{\sqrt{B^2 + AB} - B}{A}, \quad (28)$$

where $A = |\bar{\beta}\beta_0|^2[1 - \mu(0, u)]\mu(0, u)E_s + N_0[|\beta_0|^2(K - |\mathcal{G}|) - |\mathcal{U}||\bar{\beta}|^2]$ and $B = N_0|\mathcal{U}||\bar{\beta}|^2 + N_0(K - |\mathcal{G}|)/E_s$. Note that if \hat{g} cannot be updated based on (28) to meet the spectral mask bound, then the reference power has to be reduced to $\min\{E_r^{\text{opt}}, |\hat{\mathcal{G}}|\bar{E}\}$.

From (26), it can be verified that the power of the interference term decreases with u while that of the noise term increases with u . Thus u provides a trade-off between ICI suppression and noise enhancement. While finding a closed form expression for $C^{\text{LB}2}(\beta)$ -maximizing u (for given E_r, \hat{g}) is intractable, it can be computed numerically by performing a simple line search of $C^{\text{LB}2}(\beta)$ over the range $0 \leq u \leq [\min\{K_1, K_2\} - \hat{g}]/2$.

VII. PLL BASED PHASE-NOISE MODELS

In contrast to the Wiener PhN model in Section II, in this section we explore the more practical PLL based PhN models. In PLL based carrier synthesis, a high frequency VCO is locked to a stable, low frequency, low PhN crystal oscillator (XO) via a frequency division operation, as shown in Fig. 4a. Under the widely used linear approximation for the phase detector, the Laplace transform of the steady-state PhN of the PLL output $\theta_{\text{pll}}(s)$ satisfies [57]:

$$s\theta_{\text{pll}}(s) = G_{\text{pll}}\mathcal{L}(s) \left[\theta_{\text{xo}}(s) - \frac{\theta_{\text{pll}}(s)}{N} \right] + W_{\text{vco}}(s) \quad (29)$$

where, G_{pll} is the PLL open-loop gain, $\mathcal{L}(s)$ is the PLL loop low-pass filter, $N = f_c/f_{\text{xo}}$ is the ratio of carrier frequency f_c to the XO frequency f_{xo} , $W_{\text{vco}}(s)$ is Laplace transform of the VCO input noise $w_{\text{vco}}(t)$, and $\theta_{\text{xo}}(s)$ is the Laplace transform of the XO PhN $\theta_{\text{xo}}(t)$. We adopt the PhN models in [57], where $\theta_{\text{xo}}(t), w_{\text{vco}}(t)$ are Gaussian processes with power spectral densities of $S_{\text{xo}}(f) = \text{PSD}_0^{\text{xo}} \frac{1+f^2}{1+(f/\hat{f}_p)^2}$ and $S_{\text{vco}}(f) = \text{PSD}_0^{\text{vco}}$, respectively, and we assume a 1st order loop filter $\mathcal{L}(s) = \frac{2\pi f_{\text{LPF}}}{2\pi f_{\text{LPF}} + s}$ with cut-off frequency f_{LPF} . For a typical low PhN XO ($f_{\text{xo}} = 100\text{MHz}$, $\hat{f}_z = 4\text{KHz}$, $\text{PSD}_0^{\text{xo}} = -160\text{dBc/Hz}$) [57], a low PhN 90GHz VCO ($\text{PSD}_0^{\text{xo}} = 25\text{dBc/Hz}$) [58] and open-loop gain $G_{\text{pll}} = 104\text{dB}$, the 2nd-moment of the nDFT coefficients $\{\Omega_k^{\text{pll}} | k \in \mathcal{K}\}$ of $e^{j\theta_{\text{pll}}(nT_s/K)}$ are studied in Fig. 4b for different f_{LPF} values. As evident from the results, in comparison to the free running VCO, the PLL suppresses the low frequency PhN coefficients $\{\Omega_k^{\text{pll}} | |k| \leq f_{\text{LPF}}T_s\}$ but causes spectral regrowth for higher frequency nDFT coefficients. Since the proposed PhN compensation algorithm estimates and suppresses PhN in the

low frequency coefficients $|k| \leq u$, a PLL with $f_{\text{LPF}} > u/T_s$ can be detrimental to its performance, as explored in more detail in Section VIII.

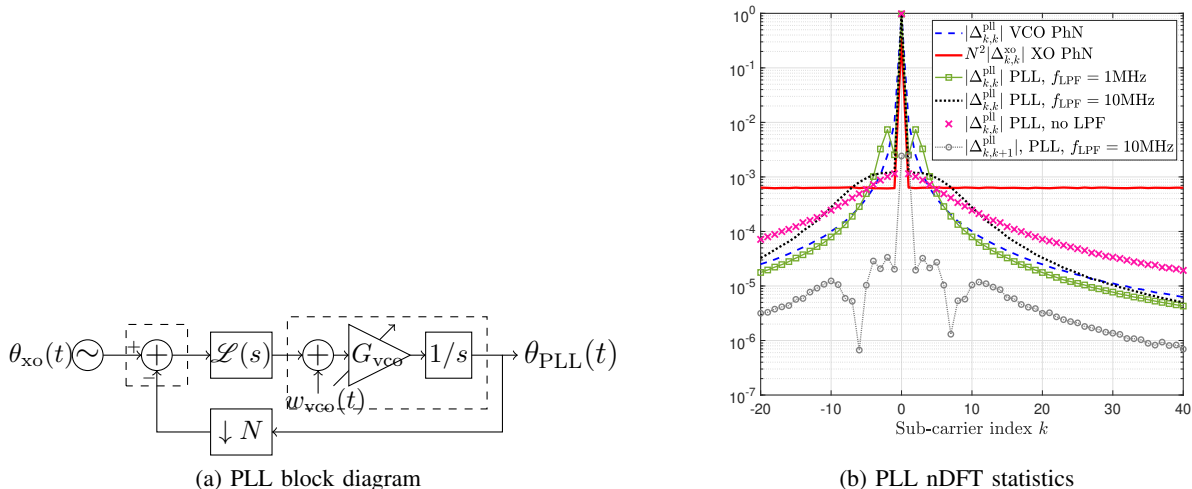


Fig. 4. Block diagram of PLL and 2nd order statistics of nDFT coefficients.

In Fig. 4b, we also plot the cross-covariance terms of the nDFT coefficients $\Delta_{k,k+1}^{\text{pll}} = \mathbb{E}\{\Omega_k^{\text{pll}}[\Omega_{k+1}^{\text{pll}}]^*\}$, which are significantly lower than the 2nd moment values. Thus the PLL based PhN also approximately satisfies $\Delta_{k_1,k_2} = 0$ for $k_1 \neq k_2$. Note that, while the analysis in the previous sections relies on $\Delta_{k_1,k_2} = 0$ for $k_1 \neq k_2$, it does not depend on the explicit value for $k_1 = k_2$. We therefore hypothesize that the presented analysis is also valid for PLL based PhN models, after appropriately replacing the value of $\Delta_{k,k}$ by $\Delta_{k,k}^{\text{pll}}$. This hypothesis is validated via simulations in Section VIII. Note that $\{\Delta_{k,k}^{\text{pll}} | k \in \mathcal{K}\}$ only depend on the RX circuit parameters and can thus be computed apriori.

VIII. SIMULATION RESULTS

For the simulations, we consider a single cell THz system with a $\lambda/2$ -spaced 32×8 ($M_{\text{tx}} = 256$) antenna TX and a representative RX sub-array with a $\lambda/2$ -spaced 4×2 ($\bar{M}_{\text{rx}} = 8$) antenna panel. We also assume perfect timing synchronization between the TX and RX. Using prior statistical channel knowledge, the TX and RX beamform along the strongest channel MPC, i.e. $\mathbf{t} = \mathbf{a}_{\text{tx}}(\bar{l}) / |\mathbf{a}_{\text{tx}}(\bar{l})|$ and $\mathbf{r} = \mathbf{a}_{\text{rx}}(\bar{l}) / |\mathbf{a}_{\text{rx}}(\bar{l})|$ for $\bar{l} = \text{argmax}_{\ell}\{|\alpha_{\ell}|\}$. The TX transmits one spatial OFDM data stream with $T_s = 1\mu\text{s}$, $K_1 = K_2 + 1 = 512$ and transmits the length 11 Barker sequence for the RS ($\hat{g} = 5$). The TX and RX are both assumed to have $f_c = 90\text{GHz}$ oscillators with PhN modeled as a Wiener processes (unless otherwise specified), having variances of $\sigma_{\theta,\text{tx}}^2 = \sigma_{\theta,\text{rx}}^2 = 0.1/T_s$ (i.e., -103 dBc/Hz at 10MHz offset) [58]. The RX is assumed to have perfect knowledge of β, N_0 and $\sigma_{\theta}^2 = \sigma_{\theta,\text{tx}}^2 + \sigma_{\theta,\text{rx}}^2$. To enable

easy reproduction of the results, we first consider a sample channel matrix $\mathbf{H}(t)$ with $\tilde{L} = 3$ MPCs, $\hat{\tau}_\ell = \{0, 20, 40\}$ ns, angles of arrival $\psi_{\text{azi}}^{\text{rx}} = \{0, \pi/10, -\pi/10\}$, $\psi_{\text{ele}}^{\text{rx}} = \{0.45\pi, \pi/2, 0.4\pi\}$ and effective amplitudes $\alpha_\ell \mathbf{a}_{\text{tx}}(\ell)^\dagger \mathbf{t} = \{\sqrt{0.6}, -\sqrt{0.3}, \sqrt{0.1}\}$. Performance comparison under more practical channel models is considered later in the section. For the numerical results, the SINR Γ_k for sub-carrier k is estimated, via Monte-Carlo iterations, as the inverse mean-square distance of the un-biased, soft decoded data-symbols from the transmitted constellation points. Note that this SINR definition is equivalent to the inverse square of the signal error vector magnitude. This SINR is further used to numerically approximate the ergodic capacity as $\sum_{k \in \mathcal{K} \setminus \mathcal{G}} \log(1 + \Gamma_k)/K$. The results are presented as a function of the average post beamforming SNR: $E_s |\beta_{\text{rms}}|^2 / N_0 K$, where we define $|\beta_{\text{rms}}|^2 \triangleq \sum_k |\beta_k|^2 / K$.

1) *Validating analytical results:* For the aforementioned channel model, the second moments of the signal, interference and noise components S_k, I_k, Z_k are compared to their analytical bounds (15)-(20) in Fig. 5a. As observed from Fig. 5a, the bounds on $\mathbb{E}\{|S_k|^2\}, \mathbb{E}\{|Z_k|^2\}$ are accurate $\forall k$. While the upper bound to $\mathbb{E}\{|I_k|^2\}$ in (17) is loose for the smaller sub-carriers, i.e., for $|k| \approx 1$, the use of Remark (IV.1) reduces the gap. The remaining residual gap in $\mathbb{E}\{|I_k|^2\}$ only impacts a few sub-carriers and thus has a negligible impact on the overall system performance. For the same system settings, the SINR for the different sub-carriers are studied as a function of SNR in Fig. 5b. We observe that the approximate SINR lower bound Γ_k^{LB} is slightly higher than the simulated SINR for $|k| \gg 1$ due to the inaccuracy of approximations in (10). However the impact of the mismatch on system capacity is negligible as shall be shown next.

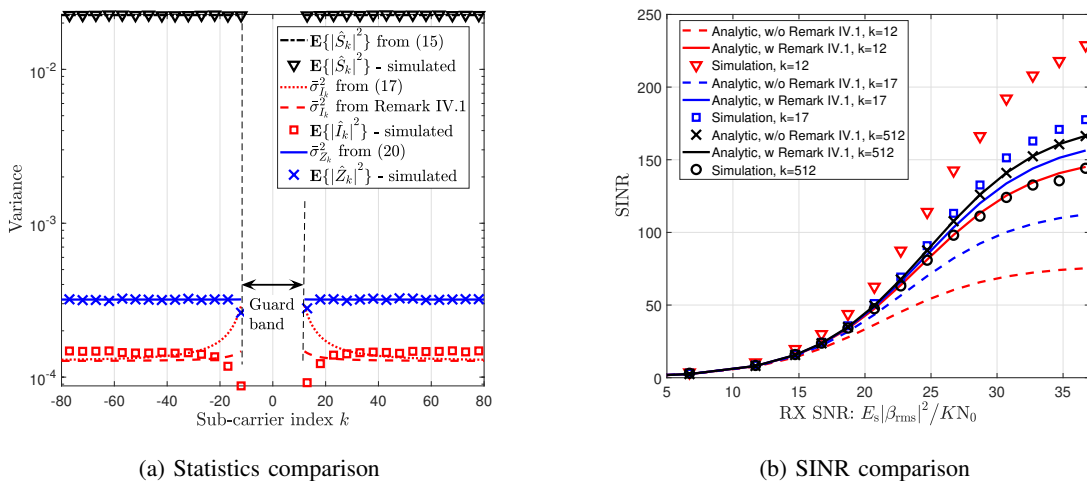


Fig. 5. Comparison of the analytical and simulated values of (a) $\mathbb{E}\{|S_k|^2\}, \mathbb{E}\{|I_k|^2\}, \mathbb{E}\{|Z_k|^2\}$ for $E_s |\beta_{\text{rms}}|^2 / (N_0 K) = 20$ dB and (b) Γ_k for varying SNR. We use $u = 3, g = 11, \sigma_\theta^2 = 0.2/T_s, E_r = 0.1E_s$ and use 16-QAM modulated data symbols for simulations.

2) *Optimal RS parameters:* We next study the impact of the parameters u, E_r on the system capacity in Fig. 6. Here, while $\mathbf{p}/\|\mathbf{p}\|$ and \hat{g} are held constant, we vary g as $g = \hat{g} + 2u$ (see Section VI) and use the throughput-optimal E_r from both: (i) (28) and (ii) brute-force search for simulations. As observed from the results, capacity changes unimodally with u . While the low capacity at lower u is due to the PhN induced ICI, the poor performance at high u is due to noise accumulation and null sub-carrier overhead. We also note that the throughput-optimal u increases with SNR. Additionally, we observe that (23) and (28) provide a very good match to the simulated capacity and optimal power allocation for each u , and the analytically optimal u coincides with the simulated optimal u , thus validating the analysis in Section VI. We also include in Fig. 6, the performance of the RX when each entry of the RS \mathbf{p} is picked randomly from the 16QAM alphabet. As evident from the results, the optimal design of the RS suggested in Section VI provides significant gains over an arbitrarily picked RS.

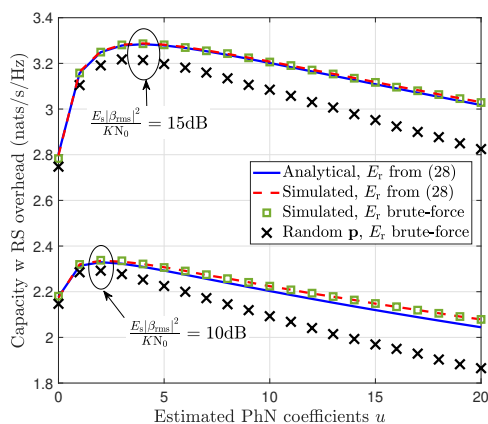


Fig. 6. Comparison of the analytical and simulated values of capacity versus u with optimal E_r . We use $\sigma_\theta^2 = 0.2/T_s, \bar{E} = E_s$, and we use 16-QAM modulated data symbols for numerically computing capacity.

3) *LMMSE estimation and frequency offset:* Next, we compare the symbol error rate (SER) of the system as a function of SNR in Fig. 7 for both LS and LMMSE based PhN estimators for (11). Here, while E_r, \hat{g}, g are held fixed, we use (i) $u = 12$ for LMMSE estimator and (ii) use $u = u^{\text{opt}}$ for the LS estimator, where u^{opt} is obtained for each SNR value by a line search over $u \in [0, 12]$ as discussed in Section VI. The results show that by optimally selecting u , the noise accumulation of the LS estimator can be controlled, thus achieving almost identical performance to the LMMSE estimator. While we assumed the TX and RX oscillators to be frequency aligned in Section II, in Fig. 7 we also depict the performance of an RX with a 1 MHz oscillator frequency mismatch. As is evident, the proposed PhN mitigation technique also provides good performance and outperforms LMMSE if there exists an oscillator frequency mismatch

smaller than u^{opt}/T_s . In other words, it is more resilient to PhN modeling errors than LMMSE.

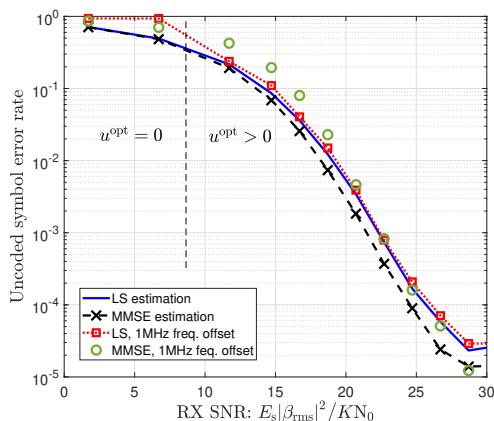


Fig. 7. Comparison of SER (averaged over data sub-carriers) versus SNR for LS and LMMSE estimation of PhN. We use $g = 30$, $\sigma_\theta^2 = 0.2/T_s$, $E_r = 0.01E_s$, $u = 12$ for LMMSE, $u \in [0, 12]$ for LS and we use 16QAM modulated data symbols for simulations.

4) *PLL based PhN models*: Next we study the accuracy of the analytical results for the PLL based PhN models in Fig. 8, for varying system parameters u , E_r . Here, while $\mathbf{p}/\|\mathbf{p}\|$ and \hat{g} are held constant, we vary g as $g = \hat{g} + 2u$ and use throughput-optimal E_r from both: (i) (28) and (ii) brute-force search for simulations. The PLL models used are identical to Section VII. As observed from the results, (23) and (28) provides a very good match to simulated results and the analytically optimal E_r , u coincide with the simulated optimal E_r , u , thus validating the applicability of our analysis to PLL based PhN models. We also observe that the optimal u increases and the maximum achievable capacity decreases for large PLL filter cut-off frequencies f_{LPF} . These observations are in line with the argument in section VII, that an oscillator with a higher power concentration in lower frequency PhN coefficients is preferred by the proposed PhN technique. In contrast, we observe that for $u = 0$ (i.e., for CPE only correction used by 3GPP NR Rel 15), a higher f_{LPF} frequency is preferable. Thus, the optimal design for the PLL can be significantly different depending on the PhN compensation approach used. A detailed analytical study of the optimal choice of f_{LPF} for a given u shall be explored in future work.

5) *Comparison to other schemes*: Finally, in Fig. 9 we compare the performance of (i) our optimized PhN estimation technique to (ii) PhN estimation with sinusoidal RS ($\hat{g} = 0$) [27], (iii) current 3GPP style CPE estimation [35], (iv) Iterative decision feedback based PhN estimation [6], [16] and (v) system with no PhN (an SER lower bound), under the UMa LoS 3GPP Rel. 15 channel model [59]. Additionally, we also include the performance of (vi) cyclic prefix aided single carrier transmission with symbol duration T_s/K and time domain PhN estimation. Here we use the PLL based PhN model from Section VII with

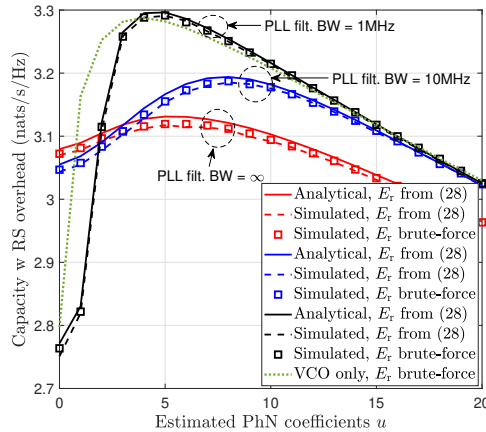


Fig. 8. Comparison of the analytical and simulated values of capacity versus u for PLL based PhN. We use $\bar{E} = E_s$, PLL parameters from Section VII and we use 16-QAM modulated data symbols for numerically computing capacity.

$f_{\text{LPF}} = 10\text{MHz}$, which is a favorable choice for CPE only estimation. While the schemes (i), (ii), (v) do not require channel estimates prior to PhN estimation, for schemes (iii), (iv) and (vi) we assume a priori perfect channel estimates. We also assume $u \in [0, 20]$, g and E_r for schemes (i) and (ii) are designed in accordance to Section VI, and the same values of u as scheme (i) are used for scheme (iv). A per sub-carrier spectral mask limit of $\bar{E} = 5/K$ is considered, that limits the pilot/reference signal boosting. To keep the pilot + null sub-carrier overhead comparable across schemes, we use 30 uniformly-spaced pilot sub-carriers, each with power \bar{E} for schemes (iii) and (iv), while for scheme (ii) we use a single RS with power \bar{E} . For scheme (vi), use 30 uniformly spaced pilots of energy E_s/K in every K symbols, the RX estimates PhN phase at pilot symbols after zero-forcing channel equalization, and uses piece-wise linear phase interpolation to obtain PhN phase at data symbols. For these schemes, the SERs with uncoded 16QAM and 64QAM transmission, averaged over sub-carriers and channel realizations, are presented in Fig. 9a and Fig. 9b, respectively.

For 16QAM, we observe that schemes (i) and (vi) significantly outperform (ii), (iii) and perform as well as (iv) while only requiring a fraction of the computational effort. For 64QAM, the optimized scheme (i) outperforms all other schemes and is reasonably close to the no PhN limit (v). Here, while the performance of scheme (ii) is limited by the RS power due to spectral mask regulations, scheme (iii) is limited by the ICI due to symbol distortion, scheme (iv) achieves only limited performance improvement over (iii) even after two decision feedback iterations due to the noise accumulation and scheme (vi) suffers from the sub-optimality of linear interpolation. While not depicted here for brevity, the relative performance of scheme (vi) degrades further in non-line-of-sight channels due to the high ISI between

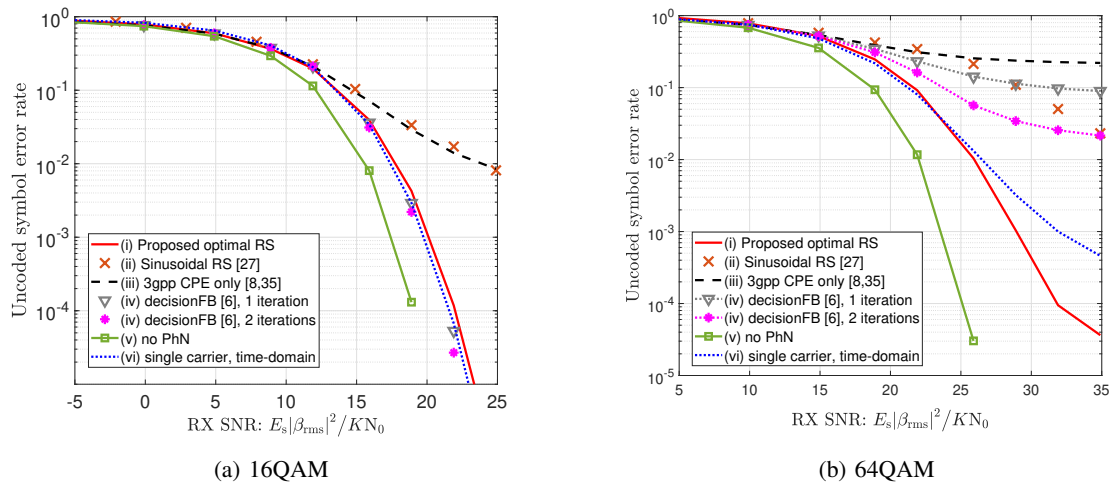


Fig. 9. Comparison of SER (averaged over data sub-carriers) versus SNR for different PhN compensation schemes (i)–(vi). We use $\bar{E} = 5/K$, PLL parameters from Section VII and we use $\psi_{azi}^{tx} = \psi_{azi}^{rx} = 0$ and $\psi_{ele}^{tx} = \psi_{ele}^{rx} = \pi/2$ for LoS path.

data and pilot symbols. Thus, with appropriate PhN mitigation, multi-carrier systems can match, and possibly out-perform, single carrier systems even in PhN limited regime. Overall, we observe that the proposed optimized PhN compensation technique outperforms several existing solutions, while providing low complexity and low latency in decoding.

IX. CONCLUSION

This paper proposes a novel RS-aided PhN estimation and mitigation technique for multi-antenna multi-carrier high frequency systems, wherein the RS is packed compactly in the frequency domain and is separated from data by null sub-carriers. The frequency concentration of the RS helps decouple PhN estimation from channel estimation and also helps keep the null sub-carrier overhead low, while the null sub-carriers prevent the interference between the RS and data. The detailed mathematical analysis shows that the low frequency components of the PhN are its principal components, and can be estimated using the received sub-carriers in the vicinity of the RS. The analysis also shows that a trade-off exists between the ICI and noise accumulation for the proposed scheme, which can be realized by varying the estimated number of PhN principal components. Furthermore, we conclude that throughput-optimal designs for the RS in the frequency domain include aperiodic ZCZSs and Barker sequences. We also conclude that a lower (higher) PLL loop bandwidth is preferable when $u > 0$ ($u = 0$). Simulations support the analytical results and show that by adapting the number of estimated PhN components, the LS PhN estimator achieves near identical performance to the MMSE estimator. The results also show that the proposed technique can compensate for small frequency offsets between the TX and RX oscillators. Simulations

further show that the proposed PhN compensation technique outperforms several other existing PhN techniques, including some single-carrier schemes.

APPENDIX A

Proof of Lemma 1. The periodicity follows directly from the fact that $\Omega_k = \Omega_{k+K}$. Note that from the definition of Ω_k , we also have $e^{-j\theta[n]} \xrightarrow{\mathcal{F}} \Omega_k$ and $e^{j\theta[n]} \xrightarrow{\mathcal{F}} \Omega_{-k}^*$, where \mathcal{F} represents the nDFT Operation. Then using convolution property of the nDFT, we have:

$$\begin{aligned} e^{-j\theta[n]} e^{j\theta[n]} &\xrightarrow{\mathcal{F}} \sum_{a \in \mathcal{K}} \Omega_a \Omega_{a+k}^* \\ &\Rightarrow 1 \xrightarrow{\mathcal{F}} \sum_{a \in \mathcal{K}} \Omega_a \Omega_{a+k}^* \\ &\Rightarrow \delta_{0,k}^K = \sum_{a \in \mathcal{K}} \Omega_a \Omega_{a+k}^* \end{aligned}$$

which proves property (6a). Property (6c) can be obtained as follows:

$$\begin{aligned} \Delta_{k_1, k_2} &= \mathbb{E}\{\Omega_{k_1} \Omega_{k_2}^*\} = \frac{1}{K^2} \sum_{\dot{n}, \ddot{n}=0}^{K-1} \mathbb{E}\{e^{-j[\theta[\dot{n}]-\theta[\ddot{n}]]}\} e^{-j2\pi \frac{[k_1 \dot{n} - k_2 \ddot{n}]}{K}} \\ &\stackrel{(1)}{=} \frac{1}{K^2} \sum_{\dot{n}, \ddot{n}=0}^{K-1} e^{-\frac{\sigma_\theta^2 |\dot{n} - \ddot{n}| T_s}{2K}} e^{-j2\pi \frac{[k_1 \dot{n} - k_2 \ddot{n}]}{K}} \\ &\stackrel{(2)}{=} \frac{1}{K^2} \sum_{\ddot{n}=0}^{K-1} \sum_{u=-\ddot{n}}^{K-1-\ddot{n}} e^{-\frac{\sigma_\theta^2 |u| T_s}{2K}} e^{-j2\pi \frac{[k_1 u + (k_1 - k_2) \ddot{n}]}{K}} \\ &\stackrel{(3)}{\approx} \frac{1}{K^2} \sum_{\ddot{n}=0}^{K-1} \sum_{u=-K/2}^{K/2-1} e^{-\frac{\sigma_\theta^2 |u| T_s}{2K}} e^{-j2\pi \frac{[k_1 u + (k_1 - k_2) \ddot{n}]}{K}} \\ &\stackrel{(4)}{=} \frac{\delta_{k_1, k_2}^K}{K} \left[\frac{1 - e^{-\left(\frac{\sigma_\theta^2 T_s - j4\pi k_1}{4}\right)}}{e^{\frac{\sigma_\theta^2 T_s - j4\pi k_1}{2K}} - 1} + \frac{1 - e^{-\left(\frac{\sigma_\theta^2 T_s + j4\pi k_1}{4}\right)}}{1 - e^{-\frac{\sigma_\theta^2 T_s + j4\pi k_1}{2K}}} \right] \end{aligned}$$

where $\stackrel{(1)}{=}$ follows by using the expression for the characteristic function of the Gaussian random variable $\theta[\dot{n}] - \theta[\ddot{n}]$; $\stackrel{(2)}{=}$ follows by defining $u = \dot{n} - \ddot{n}$ and $\stackrel{(3)}{\approx}$ follows by changing the inner summation limits which is accurate for $\sigma_\theta^2 T_s \gg 1$ and $\stackrel{(4)}{=}$ follows from the expression for the sum of a geometric series. \square

APPENDIX B

Proof of Lemma 2. Consider the denominator terms in (6c) $\kappa_1(k) \triangleq e^{\frac{\sigma_\theta^2 T_s - j4\pi k}{2K}} - 1$ and $\kappa_2(k) \triangleq 1 - e^{-\frac{\sigma_\theta^2 T_s + j4\pi k}{2K}}$. Then we have:

$$|\kappa_1(k)| = \sqrt{e^{\frac{\sigma_\theta^2 T_s}{K}} + 1 - e^{\frac{\sigma_\theta^2 T_s}{2K}} \cos\left(\frac{2\pi k}{K}\right)} \quad (30a)$$

$$|\kappa_2(k)| = \sqrt{e^{-\frac{\sigma_\theta^2 T_s}{K}} + 1 - e^{-\frac{\sigma_\theta^2 T_s}{2K}} \cos\left(\frac{2\pi k}{K}\right)} \quad (30b)$$

$$\text{Re}\{\kappa_1(k)^* \kappa_2(k)\} = \cos\left(\frac{2\pi k}{K}\right) \left[e^{\frac{\sigma_\theta^2 T_s}{2K}} - e^{-\frac{\sigma_\theta^2 T_s}{2K}} \right] \quad (30c)$$

Using (30), it can readily be shown that since $\cos(2\pi k/K)$ is a decreasing function of $|k|$ for $0 \leq |k| \leq K/2$, so is $|\kappa_1(k)^{-1} + \kappa_2(k)^{-1}|$. Now since the numerators in (6c) are the same for all even k and for all odd k , respectively, the lemma follows. \square

Corollary 1. *Using Lemma 2 we further have:* $\sum_{k \in \mathcal{K} \setminus \mathcal{G}} \eta(k, \hat{g} + u) \leq 2(1 - \mu(0, u))$.

Proof.

$$\begin{aligned} \sum_{k \in \mathcal{K} \setminus \mathcal{G}} \eta(k, \hat{g} + u) &= \sum_{k \in \mathcal{K} \setminus \mathcal{G}} \max_{0 \leq |a| \leq \hat{g} + u} \left\{ \Delta_{k+a, k+a} \right\} \\ &\stackrel{(1)}{=} \sum_{\substack{k=-K/2 \\ k \notin \mathcal{G}}}^{K/2-1} \max_{0 \leq |a| \leq \hat{g} + u} \left\{ \Delta_{k+a, k+a} \right\} \\ &\stackrel{(2)}{\leq} \sum_{\substack{k=-K/2 \\ k \notin \mathcal{G}}}^{-1} \left[\Delta_{k+\hat{g}+u, k+\hat{g}+u} + \Delta_{k+\hat{g}+u-1, k+\hat{g}+u-1} \right] \\ &\quad + \sum_{\substack{k=0 \\ k \notin \mathcal{G}}}^{K/2-1} \left[\Delta_{k-\hat{g}-u, k-\hat{g}-u} + \Delta_{k-\hat{g}-u+1, k-\hat{g}-u+1} \right] \\ &\stackrel{(3)}{\leq} \sum_{\substack{k \in \mathcal{K} \\ |k| > u}} 2\Delta_{k,k} = 2(1 - \mu(0, u)) \end{aligned} \quad (31)$$

where $\stackrel{(1)}{=}$ follows from periodicity of Ω_k and $\Delta_{k,k}$ (see Lemma 1), $\stackrel{(2)}{\leq}$ from the use of Lemma 2 and $\stackrel{(3)}{\leq}$ from the fact that $g \geq \hat{g} + 2u$ (see Section III-A). \square

APPENDIX C

$C^{\text{LB1}}(\boldsymbol{\beta})$ in (23) can further be lower bounded as:

$$\begin{aligned} C^{\text{LB1}}(\boldsymbol{\beta}) &\geq \frac{1}{K} \sum_{k \in \mathcal{K} \setminus \mathcal{G}} \log \left[\frac{|\beta_0 \beta_k|^2 E_d \mu(0, u)^2}{\bar{\sigma}_{I_k}^2 + \bar{\sigma}_{Z_k}^2} \right] \\ &\stackrel{(1)}{\geq} \sum_{k \in \mathcal{K} \setminus \mathcal{G}} \frac{\log(|\beta_0 \beta_k|^2 \mu(0, u)^2)}{K} - \frac{(K - |\mathcal{G}|)}{K} \log \left[\frac{1}{K - |\mathcal{G}|} \sum_{k \in \mathcal{K} \setminus \mathcal{G}} \left(\frac{\bar{\sigma}_{I_k}^2 + \bar{\sigma}_{Z_k}^2}{E_d} \right) \right] \end{aligned} \quad (32)$$

where $\stackrel{(1)}{\geq}$ is obtained by sending the summation into the denominator of the logarithm and using Jensen's inequality. Furthermore, using (15)-(20) we have:

$$\begin{aligned} &\frac{1}{K - |\mathcal{G}|} \sum_{k \in \mathcal{K} \setminus \mathcal{G}} \bar{\sigma}_{I_k}^2 + \bar{\sigma}_{Z_k}^2 \\ &= \frac{1}{K - |\mathcal{G}|} \sum_{k \in \mathcal{K} \setminus \mathcal{G}} \left[\sum_{\hat{k} \in \hat{\mathcal{G}}} |p_{\hat{k}}|^2 |\beta_0|^4 \tilde{\mu}(k - \hat{k}, u) + |\beta_0 \bar{\beta}|^2 E_d [\mu(0, u) - \mu(0, u)^2] \right. \\ &\quad \left. + \left[\eta_{k, \hat{g}+u}(2u+1) + \mu(0, u) \right] |\beta_0|^2 N_0 + \text{Tr}\{\mathbf{R}_p^{-1}\} N_0 \left[|\bar{\beta}|^2 E_d + N_0 \right] \right] \end{aligned} \quad (33)$$

$$\begin{aligned} &\stackrel{(2)}{\leq} \frac{1}{K - |\mathcal{G}|} \left(\sum_{\hat{k} \in \hat{\mathcal{G}}} |p_{\hat{k}}|^2 \right) |\beta_0|^4 \mu(0, u) [1 - \mu(0, u)] + |\beta_0 \bar{\beta}|^2 E_d \mu(0, u) [1 - \mu(0, u)] \\ &\quad + \left(\frac{2(2u+1)}{K - |\mathcal{G}|} [1 - \mu(0, u)] + \mu(0, u) \right) |\beta_0|^2 N_0 + \text{Tr}\{\mathbf{R}_p^{-1}\} N_0 \left[|\bar{\beta}|^2 E_d + N_0 \right] \end{aligned} \quad (34)$$

$$\stackrel{(3)}{\leq} \frac{1}{K - |\mathcal{G}|} E_s |\beta_0 \bar{\beta}|^2 \mu(0, u) [1 - \mu(0, u)] + |\beta_0|^2 N_0 + \text{Tr}\{\mathbf{R}_p^{-1}\} N_0 \left[|\bar{\beta}|^2 E_d + N_0 \right] \quad (35)$$

where $\stackrel{(2)}{\leq}$ follows by using definition of $\tilde{\mu}(\cdot)$ and $g \geq \hat{g} + 2u$ for the first term and by using Corollary 1 (from Appendix B) for the third term; and $\stackrel{(3)}{\leq}$ follows by using $E_s = E_r + (K - |\mathcal{G}|)E_d$ for the first two terms and by assuming $4u \ll K - |\mathcal{G}|$ for the third term. Note that since $g \geq 2u + \hat{g}$, this assumption is equivalent to $|\mathcal{G}| \leq K/2$ i.e., at least 50% of sub-carriers carry data, which is reasonable. Using (32) and (35), (25) follows.

REFERENCES

- [1] Cisco, "Global mobile data traffic forecast update, 2017-2022," tech. rep., Cisco Visual Networking Index, Feb. 2019. White Paper.

- [2] I. Galton and C. Weltin-Wu, "Understanding phase error and jitter: Definitions, implications, simulations, and measurement," *IEEE Transactions on Circuits and Systems I: Regular Papers*, vol. 66, pp. 1–19, jan 2019.
- [3] R. Krishnan, M. R. Khanzadi, N. Krishnan, A. G. i Amat, T. Eriksson, N. Mazzali, and G. Colavolpe, "On the impact of oscillator phase noise on the uplink performance in a massive MIMO-OFDM system," *CoRR*, vol. abs/1405.0669, 2014.
- [4] A. K. Papazafeiropoulos, "Impact of general channel aging conditions on the downlink performance of massive MIMO," *IEEE Transactions on Vehicular Technology*, vol. 66, pp. 1428–1442, feb 2017.
- [5] L. Piazza and P. Mandarini, "Analysis of phase noise effects in OFDM modems," *IEEE Transactions on Communications*, vol. 50, pp. 1696–1705, oct 2002.
- [6] S. Wu and Y. Bar-Ness, "A phase noise suppression algorithm for OFDM-based WLANs," *IEEE Communications Letters*, vol. 6, pp. 535–537, dec 2002.
- [7] S. Wu, P. Liu, and Y. Bar-Ness, "Phase noise estimation and mitigation for OFDM systems," *IEEE Transactions on Wireless Communications*, vol. 5, pp. 3616–3625, December 2006.
- [8] 3GPP, "NR: Physical channels and modulation (release 15)," Tech. Rep. TS 38.211, Technical Specification Group Radio Access Network, Dec. 2018. V15.4.0.
- [9] A. Pitarokoilis, S. K. Mohammed, and E. G. Larsson, "Effect of oscillator phase noise on uplink performance of large MU-MIMO systems," in *Annual Allerton Conference on Communication, Control, and Computing (Allerton)*, IEEE, oct 2012.
- [10] A. Puglielli, G. LaCaille, A. M. Niknejad, G. Wright, B. Nikolic, and E. Alon, "Phase noise scaling and tracking in OFDM multi-user beamforming arrays," in *IEEE International Conference on Communications (ICC)*, IEEE, may 2016.
- [11] R. Corvaja, A. G. Armada, M. A. Vazquez, and A. Perez-Neira, "Design of pre-coding and combining in hybrid analog-digital massive MIMO with phase noise," in *European Signal Processing Conference (EUSIPCO)*, IEEE, aug 2017.
- [12] V. V. Ratnam and A. F. Molisch, "Periodic analog channel estimation aided beamforming for massive MIMO systems," *IEEE Transactions on Wireless Communications*, vol. 18, pp. 1581–1594, mar 2019.
- [13] V. V. Ratnam and A. Molisch, "Multi-antenna FSR receivers: Low complexity, non-coherent, massive antenna receivers," in *IEEE Global Communications Conference (GLOBECOM)*, Dec. 2018.
- [14] V. V. Ratnam and A. F. Molisch, "Continuous analog channel estimation aided beamforming for massive MIMO systems," *CoRR*, vol. abs/1901.08763, 2019.
- [15] S. Bittner, E. Zimmermann, and G. Fettweis, "Iterative phase noise mitigation in MIMO-OFDM systems with pilot aided channel estimation," in *IEEE Vehicular Technology Conference*, IEEE, sep 2007.
- [16] D. Petrovic, W. Rave, and G. Fettweis, "Effects of phase noise on OFDM systems with and without PLL: Characterization and compensation," *IEEE Transactions on Communications*, vol. 55, pp. 1607–1616, Aug 2007.
- [17] Q. Zou, A. Tarighat, and A. H. Sayed, "Compensation of phase noise in OFDM wireless systems," *IEEE Transactions on Signal Processing*, vol. 55, pp. 5407–5424, nov 2007.
- [18] H. Mehrpouyan, A. A. Nasir, S. D. Blostein, T. Eriksson, G. K. Karagiannidis, and T. Svensson, "Joint estimation of channel and oscillator phase noise in MIMO systems," *IEEE Transactions on Signal Processing*, vol. 60, pp. 4790–4807, sep 2012.
- [19] P. Robertson and S. Kaiser, "Analysis of the effects of phase-noise in orthogonal frequency division multiplex (OFDM) systems," in *IEEE International Conference on Communications (ICC)*, vol. 3, pp. 1652–1657 vol.3, Jun 1995.
- [20] R. Casas, S. Biracree, and A. Youtz, "Time domain phase noise correction for OFDM signals," *IEEE Transactions on Broadcasting*, vol. 48, pp. 230–236, sep 2002.
- [21] A. Leshem and M. Yemini, "Phase noise compensation for OFDM systems," *IEEE Transactions on Signal Processing*, vol. 65, pp. 5675–5686, nov 2017.

- [22] P. Rabiei, W. Namgoong, and N. Al-Dhahir, "A non-iterative technique for phase noise ICI mitigation in packet-based OFDM systems," *IEEE Transactions on Signal Processing*, vol. 58, pp. 5945–5950, nov 2010.
- [23] R. Corvaja and A. Armada, "Joint channel and phase noise compensation for OFDM in fast-fading multipath applications," *IEEE Transactions on Vehicular Technology*, vol. 58, pp. 636–643, feb 2009.
- [24] M. R. Khanzadi, R. Krishnan, and T. Eriksson, "Estimation of phase noise in oscillators with colored noise sources," *IEEE Communications Letters*, vol. 17, pp. 2160–2163, nov 2013.
- [25] M. El-Tanany, Y. Wu, and L. Hazy, "Analytical modeling and simulation of phase noise interference in OFDM-based digital television terrestrial broadcasting systems," *IEEE Transactions on Broadcasting*, vol. 47, pp. 20–31, mar 2001.
- [26] S. L. Jansen, I. Morita, N. Takeda, and H. Tanaka, "20-gb/s OFDM transmission over 4,160-km SSMF enabled by RF-pilot tone phase noise compensation," in *Optical Fiber Communication Conference and Exposition and The National Fiber Optic Engineers Conference*, p. PDP15, Optical Society of America, 2007.
- [27] S. Randel, S. Adhikari, and S. L. Jansen, "Analysis of RF-pilot-based phase noise compensation for coherent optical OFDM systems," *IEEE Photonics Technology Letters*, vol. 22, pp. 1288–1290, Sept 2010.
- [28] H. Donelan and T. O'Farrell, "Large families of ternary sequences with aperiodic zero correlation zones for a MC-DS-CDMA system," in *International Symposium on Personal, Indoor and Mobile Radio Communications*, IEEE, 2002.
- [29] C. Han, T. Hashimoto, and N. Suehiro, "Poly phase zero-correlation zone sequences based on complete complementary codes and DFT matrix," in *International Workshop on Signal Design and Its Applications in Communications*, IEEE, sep 2007.
- [30] D. Wu, P. Spasojevic, and I. Seskar, "Orthogonal variable spreading factor codes with zero-correlation zone for TS-UWB," in *Wireless Communications and Networking Conference*, IEEE, 2005.
- [31] S. Golomb and R. Scholtz, "Generalized barker sequences," *IEEE Transactions on Information Theory*, vol. 11, pp. 533–537, oct 1965.
- [32] P. Stoica, H. He, and J. Li, "New algorithms for designing unimodular sequences with good correlation properties," *IEEE Transactions on Signal Processing*, vol. 57, pp. 1415–1425, apr 2009.
- [33] A. Leukhin, V. I Parsaev, and V. Bezrodnyi, "Unimodular sequences with good aperiodic autocorrelation," in *Sequences and Their Applications*, 10 2018.
- [34] X. Chen, W. Fan, and A. Zhang, "On low-pass phase noise mitigation in OFDM system for mmWave communications," in *Communications and Networking*, pp. 271–280, Springer International Publishing, 2018.
- [35] Y. Guo, H. Yang, and Y. Zhang, "Tracking reference signal design for phase noise compensation for SC-FDMA waveform," in *IEEE International Conference on Communication Technology (ICCT)*, IEEE, oct 2017.
- [36] Y. Qi, M. Hunukumbure, H. Nam, H. Yoo, and S. Amuru, "On the phase tracking reference signal (PT-RS) design for 5g new radio (NR)," *CoRR*, vol. abs/1807.07336, 2018.
- [37] A. F. Molisch, V. V. Ratnam, S. Han, Z. Li, S. L. H. Nguyen, L. Li, and K. Haneda, "Hybrid beamforming for massive MIMO: A survey," *IEEE Communications Magazine*, vol. 55, pp. 134–141, Sept 2017.
- [38] S. Park, A. Alkhateeb, and R. W. Heath, "Dynamic subarrays for hybrid precoding in wideband mmWave MIMO systems," *IEEE Transactions on Wireless Communications*, vol. 16, pp. 2907–2920, may 2017.
- [39] M. Akdeniz, Y. Liu, M. Samimi, S. Sun, S. Rangan, T. Rappaport, and E. Erkip, "Millimeter wave channel modeling and cellular capacity evaluation," *IEEE Journal on Selected Areas in Communications*, vol. 32, pp. 1164–1179, June 2014.
- [40] X. Zhang, A. Molisch, and S.-Y. Kung, "Variable-phase-shift-based RF-baseband codesign for MIMO antenna selection," *IEEE Transactions on Signal Processing*, vol. 53, pp. 4091–4103, Nov 2005.

- [41] A. Alkhateeb, G. Leus, and R. W. Heath, "Limited feedback hybrid precoding for multi-user millimeter wave systems," *IEEE Transactions on Wireless Communications*, vol. 14, pp. 6481–6494, Nov 2015.
- [42] F. Sahrabi and W. Yu, "Hybrid digital and analog beamforming design for large-scale antenna arrays," *IEEE Journal of Selected Topics in Signal Processing*, vol. 10, pp. 501–513, April 2016.
- [43] P. Sudarshan, N. Mehta, A. Molisch, and J. Zhang, "Channel statistics-based RF pre-processing with antenna selection," *IEEE Transactions on Wireless Communications*, vol. 5, pp. 3501–3511, December 2006.
- [44] V. V. Ratnam, O. Y. Bursalioglu, H. Papadopoulos, and A. Molisch, "Preprocessor design for hybrid preprocessing with selection in massive MISO systems," in *IEEE International Conference on Communications (ICC)*, May 2017.
- [45] S. Haghighatshoar and G. Caire, "Massive MIMO channel subspace estimation from low-dimensional projections," *IEEE Transactions on Signal Processing*, vol. 65, pp. 303–318, Jan 2017.
- [46] V. Ratnam, A. Molisch, O. Y. Bursalioglu, and H. C. Papadopoulos, "Hybrid beamforming with selection for multi-user massive MIMO systems," *IEEE Transactions on Signal Processing*, pp. 1–1, 2018.
- [47] S. Park, J. Park, A. Yazdan, and R. W. Heath, "Exploiting spatial channel covariance for hybrid precoding in massive MIMO systems," *IEEE Transactions on Signal Processing*, vol. 65, pp. 3818–3832, July 2017.
- [48] A. Mehrotra, "Noise analysis of phase-locked loops," *IEEE Transactions on Circuits and Systems I: Fundamental Theory and Applications*, vol. 49, pp. 1309–1316, Sep 2002.
- [49] 3GPP, "Study on new radio access technology: Radio frequency (rf) and co-existence aspects (release 14)," Tech. Rep. TR 38.803, Technical Specification Group Radio Access Network, Sept. 2017. V14.2.0.
- [50] V. Abhayawardhana and I. Wassell, "Common phase error correction with feedback for OFDM in wireless communication," in *Global Telecommunications Conference (GLOBECOM)*, IEEE.
- [51] G. J. Foschini and M. J. Gans, "On limits of wireless communications in a fading environment when using multiple antennas," *Wireless Personal Communications*, vol. 6, pp. 311–335, Mar. 1998.
- [52] A. Goldsmith and P. Varaiya, "Capacity of fading channels with channel side information," *IEEE Transactions on Information Theory*, vol. 43, no. 6, pp. 1986–1992, 1997.
- [53] T. M. Cover and J. A. Thomas, *Elements of Information Theory 2nd Edition (Wiley Series in Telecommunications and Signal Processing)*. Wiley-Interscience, 2006.
- [54] R. Bhatia and C. Davis, "A better bound on the variance," *The American Mathematical Monthly*, vol. 107, p. 353, apr 2000.
- [55] S. W. Golomb and G. Gong, *Signal Design for Good Correlation: For Wireless Communication, Cryptography, and Radar*. Cambridge University Press, 2005.
- [56] S. Schaible, "Fractional programming," *Zeitschrift fr Operations Research*, vol. 27, pp. 39–54, dec 1983.
- [57] P. Zetterberg, A. Wolfgang, A. Westlund, M. Hunukumbure, Y. Qi, Y. Wang, P. Baracca, D. Ferling, H. Halbauer, M. Iwanow, N. Vucic, M. H. Castañeda, J. Luo, R. D'Errico, G. Dussopt, A. Clemente, T. Svensson, B. Makki, C. Fang, G. Durisi, Y. Zou, S. Armour, W. Yan, U. Gustavsson, M. Fresia, M. Honglei, D. T. P. Huy, P. Ratajczak, and H. Wang, "Initial multi-node and antenna transmitter and receiver architectures and schemes; deliverable d5.1," Tech. Rep. ICT-671650, Horizon2020, Mar. 2016.
- [58] J. Zhang, N. Sharma, W. Choi, D. Shim, Q. Zhong, and K. K. O., "85-to-127 GHz CMOS signal generation using a quadrature VCO with passive coupling and broadband harmonic combining for rotational spectroscopy," *IEEE Journal of Solid-State Circuits*, vol. 50, pp. 1361–1371, jun 2015.
- [59] TR38.900, "Study on channel model for frequency spectrum above 6 GHz (release 14)," Tech. Rep. V14.3.1, 3GPP, 2017.